

8-2018

Measuring the Vortex-Shedding Frequency Behind Staggered Cylinders in Cross-Flow

Christopher Clark

Santa Clara University, cmclark@scu.edu

Follow this and additional works at: https://scholarcommons.scu.edu/mech_mstr



Part of the [Mechanical Engineering Commons](#)

Recommended Citation

Clark, Christopher, "Measuring the Vortex-Shedding Frequency Behind Staggered Cylinders in Cross-Flow" (2018). *Mechanical Engineering Master's Theses*. 22.

https://scholarcommons.scu.edu/mech_mstr/22

This Thesis is brought to you for free and open access by the Engineering Master's Theses at Scholar Commons. It has been accepted for inclusion in Mechanical Engineering Master's Theses by an authorized administrator of Scholar Commons. For more information, please contact rscroggin@scu.edu.

SANTA CLARA UNIVERSITY

Department of Mechanical Engineering

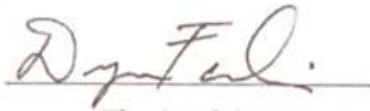
Date: August 27, 2018

I HEREBY RECOMMEND THAT THE THESIS PREPARED UNDER
MY SUPERVISION BY
Christopher Clark

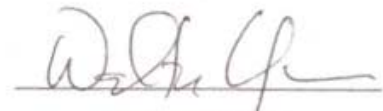
ENTITLED

**MEASURING THE VORTEX-SHEDDING FREQUENCY BEHIND STAGGERED CYLINDERS IN
CROSS-FLOW**

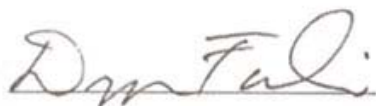
BE ACCEPTED IN PARTIAL FULFILLMENT OF THE
REQUIREMENTS FOR THE DEGREE
OF
MASTER OF SCIENCE IN MECHANICAL ENGINEERING



Thesis Advisor



Thesis Reader



Chair of Department

Measuring the Vortex-Shedding Frequency Behind Staggered Cylinders in Cross-Flow

© Christopher Clark, August 2018. All rights reserved.

Abstract

In this thesis, the Strouhal numbers from the downstream cylinder in a two cylinder configuration have been measured experimentally. Special apparatuses were designed to secure the cylinders in the wind tunnel as well as to hold a hot film anemometer probe in the center of the downstream cylinder's wake. The cylinders were smooth, of equal diameter and extended the entire width of the wind tunnel. Because the cylinders used in this thesis were sufficiently long compared to their diameters and measurements were taken at center span, they were assumed to be infinite. The anemometer was calibrated according to King's Law, enabling anemometer voltage output to be related to wind tunnel flow velocity. Power spectra were then obtained from anemometer data using FFT. The peaks from these power spectra were considered the dominant vortex-shedding frequencies in the cylinder wake and were used to calculate the Strouhal number, St . St measurements were taken for different α , the angle between cylinders relative to the flow axis and different P/D (dimensionless cylinder pitch) spacing. In this experiment, α was varied between 0 and 90° and P/D of 2, 3 and 4 were tested. In addition, measurements were taken for three Reynolds numbers in the high sub-critical regime: $Re_D = 1.70e+04$, $2.89e+04$, and $3.98e+04$. For P/D spacings of 2 and 3, the Strouhal number increased at low α to a peak value near $\alpha \approx 6 - 8^\circ$. St then decreased before increasing towards the single cylinder value at higher α , though, there was considerable scatter in $P/D = 3$ data after the peak St value. For $P/D = 4$, St monotonically increased towards the single cylinder value for all α . No discernible trend between St and Re_D was observed from $0 < \alpha < 20^\circ$ for $P/D = 2, 3$ or 4 . Additionally, there was no clear correlation between the location of peak St for $P/D = 2$ and 3 and Reynolds number Re_D . However, from $20 < \alpha < 90^\circ$, St were generally higher for all P/D with increasing Re_D . Many cylinder configurations displayed frequency doubling, or two dominant vortex-shedding frequencies, with the higher frequency measuring twice as large as the other. This indicated that the velocity signal that was obtained in the wake of the downstream cylinder was not an exact sine wave. This was confirmed by performing time-synchronous signal averaging. The presence of two modal frequencies represented in-phase vortex-shedding. Three vortex-shedding frequencies were measured for select cylinder configurations. When three modes were measured, the third was twice as large as the first, and the second mode was in between, representing out-of-phase vortex-shedding. Two modes of vortex-shedding were observed at a large number of P/D and α cylinder configurations, and three modes of vortex-shedding were found at $\alpha = 30$ and 40° for $P/D = 3$.

Keywords: Flow past a cylinder, cross-flow, vortex-shedding, time-synchronous average, Strouhal number, staggered cylinders, tandem cylinders, flow past multiple cylinders, 1st mode, 2nd mode, 3rd mode, in-phase, out-of-phase.

Acknowledgements

I would like to thank Dr. Fabris for this research opportunity and my parents and sister for their support throughout my education.

Table of Contents

Nomenclature	viii
1 Introduction	1
1.1 Background/Motivation of Subject Matter	1
1.2 Flow Past a Single Infinite Circular Cylinder	1
1.3 Flow Past Multiple Infinite Circular Cylinders	3
1.4 Literature Review	3
1.5 Objectives	5
2 Experimental Setup	7
2.1 Overview	7
2.2 Equipment Configuration	7
2.3 Cylinder Configurations	10
2.4 Thermal Anemometer Calibration	10
2.5 Testing Procedure	13
3 Experimental Results	16
3.1 Strouhal Number Measurements	16
3.2 Test Results	16
3.2.1 Time-synchronous Signal Averaging	16
3.2.2 Strouhal Number Data	22
4 Conclusion	31
References	33
Appendices	35
A Frequency Response of Thermal Anemometer	35
B Experimental Equipment	36
C Power Spectra	37
D MATLAB Code	46
D.1 Create power spectra and locate peaks	46

D.2 Create time-synchronous averages	48
------------------------------------------------	----

List of Figures

2.1 Open-circuit wind tunnel used in this experiment.	8
2.2 Side view of cylinder and probe configuration in wind tunnel test section with Pitot-static tube used to provide reference flow conditions (probe is angled rod sticking up from bottom of wind tunnel).	9
2.3 Schematic of cylinder and probe configuration in wind tunnel test section.	10
2.4 Constant temperature thermal anemometer calibration curve: correlation coefficient $r = 0.9984$	12
2.5 Close-up of the flow incidence adjusting plate.	15
3.6 Time-synchronous signal average (blue) for $P/D = 2$, $\alpha = 90^\circ$: $Re_D = 1.70e+04$, overlaid on signal noise (black). Velocity waveform is plotted for one period of oscillation.	17
3.7 Time-synchronous signal average (blue) for $P/D = 2$, $\alpha = 30^\circ$: $Re_D = 1.70e+04$, overlaid on signal noise (black). Velocity waveform is plotted for one period of oscillation.	18
3.8 Time-synchronous signal average (blue) for $P/D = 2$, $\alpha = 90^\circ$: $Re_D = 2.89e+04$, overlaid on signal noise (black). Velocity waveform is plotted for one period of oscillation.	19
3.9 Time-synchronous signal average (blue) for $P/D = 2$, $\alpha = 30^\circ$: $Re_D = 2.89e+04$, overlaid on signal noise (black). Velocity waveform is plotted for one period of oscillation.	20
3.10 Time-synchronous signal average (blue) for $P/D = 2$, $\alpha = 90^\circ$: $Re_D = 3.98e+04$, overlaid on signal noise (black). Velocity waveform is plotted for one period of oscillation.	21
3.11 Time-synchronous signal average (blue) for $P/D = 2$, $\alpha = 30^\circ$: $Re_D = 3.98e+04$, overlaid on signal noise (black). Velocity waveform is plotted for one period of oscillation.	22
3.12 St vs. α for $P/D = 3$: $Re_D = 2.89e+04$. Each power spectrum has been shifted up 10^7 from the previous power spectrum in order to present them all on the same plot. In addition, each power spectrum is the result of 5 averages.	24
3.13 St vs. α for $P/D = 4$: $Re_D = 1.70e+04$. Each power spectrum has been shifted up 10^7 from the previous power spectrum in order to present them all on the same plot. In addition, each power spectrum is the result of 5 averages.	25
3.14 St vs. α for $P/D = 2$: 1st mode (Δ , \circ , \square), 2nd/3rd mode (\blacktriangle , \bullet , \blacksquare).	27
3.15 St vs. α for $P/D = 3$: 1st mode (Δ , \circ , \square), 2nd/3rd mode (\blacktriangle , \bullet , \blacksquare).	28
3.16 St vs. α for $P/D = 4$: 1st mode (Δ , \circ , \square), 2nd/3rd mode (\blacktriangle , \bullet , \blacksquare).	29

A.1	Frequency response of hot film sensor, oscilloscope settings: $5\mu s/DIV$, 0.1 mV/DIV	35
C.2	St vs. α for $P/D = 2$: $Re_D = 1.70e+04$. Each power spectrum is the result of 5 averages.	37
C.3	St vs. α for $P/D = 2$: $Re_D = 2.89e+04$. Each power spectrum is the result of 5 averages.	38
C.4	St vs. α for $P/D = 2$: $Re_D = 3.98e+04$. Each power spectrum is the result of 5 averages.	39
C.5	St vs. α for $P/D = 3$: $Re_D = 1.70e+04$. Each power spectrum is the result of 5 averages.	40
C.6	St vs. α for $P/D = 3$: $Re_D = 2.89e+04$. Each power spectrum is the result of 5 averages.	41
C.7	St vs. α for $P/D = 3$: $Re_D = 3.98e+04$. Each power spectrum is the result of 5 averages.	42
C.8	St vs. α for $P/D = 4$: $Re_D = 1.70e+04$. Each power spectrum is the result of 5 averages.	43
C.9	St vs. α for $P/D = 4$: $Re_D = 2.89e+04$. Each power spectrum is the result of 5 averages.	44
C.10	St vs. α for $P/D = 4$: $Re_D = 3.98e+04$. Each power spectrum is the result of 5 averages.	45

List of Tables

2.1	Flow incidence angles α for which St was measured.	14
3.2	St vs. α observations.	26

Nomenclature

A	: King's Law coefficient (V^2)
AR	: aspect ratio
α	: angle between cylinders relative to the flow axis
B	: King's Law coefficient $\left(\frac{V^2}{m^{0.5}/s^{0.5}}\right)$
B'	: King's Law coefficient $\left(\frac{V^2}{m^{0.5}/s^{0.5}}\right)$
D	: cylinder diameter (m)
DFT	: Discrete Fourier Transform
δ	: momentum boundary layer thickness (m)
δ/D	: dimensionless momentum boundary layer thickness
E	: King's Law coefficient (V^2)
FFT	: Fast Fourier Transform
f	: frequency of vortex-shedding (Hz)
L	: cylinder length (m)
n	: King's Law exponent
P	: center to center pitch spacing between cylinders (m)
P/D	: pitch ratio
R	: resistance (Ω)
r	: correlation coefficient
Re_D	: Reynolds number based on cylinder diameter
St	: Strouhal number
t	: pulse width (s)
tsa	: Time-synchronous average
U	: free-stream flow velocity (m/s)
ν	: kinematic viscosity of the flow fluid (m^2/s)
x	: streamwise coordinate direction (m)
y	: cross-streamwise coordinate direction (m)

1 Introduction

1.1 Background/Motivation of Subject Matter

There are many practical engineering applications where an understanding of flow interference between multiple closely-spaced objects is critical. Some examples include the design of piers and bridges with closely-spaced members, closely grouped buildings, twin chimney stacks, heat exchanger tubes, and electrical transmission lines where wind loading is present [1]. Depending on the size and shape of the objects in addition to the flow velocity and viscosity, the flow may separate or detach at some point as it passes around the objects. The periodic separation of the flow around objects is called vortex-shedding. Vortex-shedding can result in flow-induced structural vibration and unwanted noise. Therefore, a comprehension of the scenarios in which vortex-shedding occurs is advantageous to engineering designers.

The majority of situations in which flow interaction is of importance occur between closely-spaced objects with complex geometries. It is therefore advantageous to study these interactions on simple geometries such as smooth circular cylinders so the interactions can be examined without the complexities that geometrical factors may introduce.

This thesis is a fundamental study of the wake interaction between two infinite cylinders of the same diameter in cross-flow. The effects on vortex-shedding of the downstream cylinder due to the angle between cylinders relative to the flow axis α and P/D (dimensionless cylinder pitch) spacing were investigated. In this thesis, α was varied between 0 and 90° and P/D of 2, 3 and 4 were tested. In addition, the effect of different Reynolds numbers on vortex-shedding was examined.

1.2 Flow Past a Single Infinite Circular Cylinder

A cylinder may be considered infinite if it is sufficiently long so that its ends have no effect on the flow pattern being measured. For the purposes of this paper, the infinite cylinder assumption also means that the side walls of the wind tunnel have negligible effect on the flow past the cylinder [2].

The characteristics of a flow past a cylinder which is perpendicular to the flow may be classified by the Reynolds number regime. The Reynolds number is a dimensionless number defined by the characteristic length scale (cylinder diameter D), free-stream flow velocity U , and kinematic viscosity of the flow fluid ν :

$$Re_D = \frac{UD}{\nu}. \quad (1)$$

When $Re_D \ll 1$, the inertial effects of the flow can be neglected and flow around the cylinder is described by Stokes solution [3]. In this Reynolds number regime, the flow upstream and downstream from the cylinder are identical. When $4 < Re_D < 40$ the flow separates from the cylinder and Oseen's approximation modifies Stokes solution to account for inertial effects in the flow [3]. In this region, velocity near the cylinder wall decreases due to the adverse pressure gradient (meaning that the pressure gradient $\frac{\partial p}{\partial x} > 0$) imposed on the boundary layer by the flow outside the boundary layer. At a location moving towards the rear of the cylinder, this velocity will reach zero and become negative, resulting in back flow or a re-circulation of the flow near the cylinder wall. The location where this re-circulation occurs is the separation point [2]. The result of separation is two attached eddies forming behind the cylinder, one above and one below the central axis of the cylinder. As Reynolds number increases in this regime, the flow becomes unsteady and velocity oscillates downstream of the cylinder. This flow pattern is known as the von Kármán vortex street, and is characterized by offset regions of local high vorticity, or rotating fluid that form in two rows, one above and one below the central axis behind the cylinder [2]. Tritton (1988) notes that the vortex street travels downstream at a velocity that is smaller than the free-stream velocity U [2].

From $40 < Re_D < 80$, the two eddies remain attached to the cylinder but their size grows considerably. When Re_D increases past 80, the von Kármán vortex street begins to form nearer to the cylinder and the attached eddies begin to oscillate before shedding periodically from the cylinder. While the eddy on one side of the cylinder is forming due to circulation of the fluid around the cylinder, the other eddy with opposite circulation is being shed from the cylinder [3]. Once shed, these eddies join the von Kármán vortex street [2]. The frequency at which the eddies or vortices detach from the cylinder is the vortex-shedding frequency f .

The Strouhal number is a non-dimensional number representing the vortex-shedding frequency where f is the frequency, D is the characteristic length scale (in this case cylinder diameter), and U is the free-stream flow velocity [2]:

$$St = \frac{fD}{U}. \quad (2)$$

The sub-critical Reynolds number regime is from $80 < Re_D < 3 \times 10^5$. Throughout this regime, the boundary layer remains laminar and boundary layer separation occurs near 82° from the frontal stagnation point [3]. In the high sub-critical regime, the wake may become turbulent. Within the sub-critical Reynolds number regime, 0.2 is an accurate assumption for the Strouhal number of a single smooth cylinder in cross flow [2].

From $3 \times 10^5 < Re_D < 3 \times 10^6$, the boundary layer transitions from laminar to turbulent. The turbulent boundary layer is capable of withstanding a larger adverse pressure gradient than the laminar boundary layer due to its higher energy content. As a result, the turbulent boundary layer separates near 125° from the frontal stagnation point [3].

1.3 Flow Past Multiple Infinite Circular Cylinders

As mentioned in Section 1.1, many engineering structures feature multiple closely-spaced objects that can be subjected to a flow. Each object can be treated as a separate bluff body. A bluff body is an object that does not have a streamlined geometry to minimize its wake, and therefore experiences drag forces due to boundary layer separation. When bluff bodies exist close to one another in a flow, the wake of one body may affect the wake of another. If the bodies are in such close proximity that the flow in the space between them is affected, or if the wake of one body interacts with the boundary layer of the other, then the vortex-shedding characteristics of either bluff body may be altered from those expected if either body was isolated in the flow [4].

1.4 Literature Review

Zdravkovich in 1977 divided two cylinder arrangements into three categories [1]. Tandem cylinders are located one behind the other, where the angle between cylinders relative to the flow axis is $\alpha = 0^\circ$ and side by side cylinders face the flow together one on top of the other where $\alpha = 90^\circ$. Staggered cylinders represent all arrangements with $0 < \alpha < 90^\circ$. Additionally, Zdravkovich discovered that center to center cylinder spacing has an effect on flow characteristics like Strouhal number.

Kiya *et al.* in 1980 studied the effect of the angle α and P/D spacing between two cylinders of equal diameter in cross flow on the Strouhal number [5]. The authors took measurements of the Strouhal number for one of the cylinders every 15° from $0 \leq \alpha \leq 180^\circ$. From $0 < \alpha < 90^\circ$ the measurements represented vortex-shedding from an upstream cylinder and from $90 < \alpha < 180^\circ$ they represented vortex-shedding from a downstream cylinder. Vortex-shedding frequencies were also recorded at several streamwise and cross-streamwise locations downstream of the two cylinders. It was found that the vortex-shedding frequency measured varied depending on measurement location.

Zdravkovich in 1987 decomposed multi-cylinder flow interference into four regions: proximity, wake, proximity and wake, and negligible [4]. Proximity interference occurs when cylinders are close together,

from $1 < P/D < 3.5$ and α where the downstream cylinder is not submerged in the upstream cylinder's wake. Wake interference occurs when a cylinder is near or in the wake of another. Proximity and wake interference is a combination of the two. Negligible interference occurred for P/D of about 4 and greater for side by side cylinders and for various P/D and α that did not result in the types of interference listed above.

Sumner *et al.* in 2000 used particle image velocimetry (PIV) to study the flow around two circular cylinders of equal diameter in staggered arrangements for sub-critical Reynolds numbers $850 \leq Re_D \leq 1900$ [6]. From $1.0 \leq P/D \leq 1.125$ and $0 \leq \alpha \leq 45^\circ$, instabilities in the shear layer from the upstream cylinder were observed. Between $45 \leq \alpha \leq 90^\circ$, a single low-frequency vortex-shedding process was observed. P/D spacing of 1.125 to 1.25 and $45 \leq \alpha \leq 90^\circ$, resulted in a single vortex street for the staggered cylinder arrangement. From $1.125 \leq P/D \leq 4.0$ and $0 \leq \alpha \leq 20^\circ$, the authors saw a reattachment of the inner shear layer from the upstream cylinder to the downstream cylinder. For $1.125 \leq P/D \leq 3.0$ and $10 \leq \alpha \leq 30^\circ$ the narrow region between cylinders was observed to induce separation and vortex-shedding on the inner surface of the downstream cylinder. For P/D values ranging from 1.25 to 3.5 and $20 \leq \alpha \leq 45^\circ$, the authors saw pairing of vortices with opposite signs across the gap between cylinders that was enveloped by the outer shear layer of the upstream cylinder. For P/D spacings from 1.25 to 4.0 and α from 20 to 90° , the authors also observed vortex pairing but the gap vortex pair was not completely enveloped by the outer shear layer of the upstream cylinder. From $1.5 \leq P/D \leq 5.0$ and $15 \leq \alpha \leq 90^\circ$, vortex-shedding on either side of the gap between cylinders was observed to display anti-phase synchronization. In addition, the authors observed that flow through the gap was deflected away from the free-stream axis into the wake of the downstream cylinder. This resulted in the upstream and downstream cylinders having different wake widths and vortex-shedding frequencies. Finally, the authors saw impingement of vortices from the upstream cylinder on the downstream cylinder for P/D from 3.0 to 5.0 and $0 \leq \alpha \leq 20^\circ$.

Zhou *et al.* in 2004 measured the dependence of the Strouhal number on P/D spacing and Reynolds number Re_D for tandem configurations ($\alpha = 0^\circ$) [7]. The authors experimentally found that Strouhal number increased rapidly with increasing Reynolds number when $Re_D < 1.3 \times 10^3$ and approached a constant when $Re_D > 2 \times 10^4$. For $P/D = 2, 3, 4$, they found that St decreased slightly with increasing Re_D when $Re_D > 2 \times 10^4$. They proposed that St increasing with Re_D in the $Re_D < 1.3 \times 10^3$ regime could be explained by momentum boundary layer scaling. Scaling the dimensionless form of the momentum boundary layer thickness δ/D with the Reynolds number gives Equation (3) from [2]:

$$\frac{\delta}{D} \sim \frac{1}{\sqrt{Re_D}}. \quad (3)$$

Roshko, in 1955 proposed the necessity of a "wake Strouhal number, (St^*)" which depends on the ordinary Strouhal number (St) in addition to the base pressure coefficient C_{pb} [8]. Williamson *et al.* in 1998 found this to be $St^* = 0.176$ experimentally and developed a relationship between St , St^* , and C_{pb} (see Eq. (4)) [9]:

$$St = St^* \sqrt{1 - C_{pb}} \left(1 - \frac{2\delta}{D}\right)^{-1}. \quad (4)$$

Equations (3) and (4) describe how an increase in Reynolds number results in decrease in momentum boundary layer thickness and subsequent increase in Strouhal number.

Mahbub *et al.* in 2008 used hot wires to measure vortex-shedding frequencies associated with flows around two tandem cylinders of equal diameter and P/D spacing of 6.0 [10]. Power spectral densities were recorded to determine which frequencies were present at certain locations in the flow. The authors found that in between cylinders, one dominant frequency was present, but that behind both cylinders, two peak vortex-shedding frequencies were identifiable. It was observed that when two shedding frequencies were present, one was identical to that of the upstream cylinder.

Sumner *et al.* in 2008 measured the dependence of Strouhal numbers on both P/D spacing and angle of flow incidence α between two staggered cylinders of equal diameter in cross-flow for sub-critical Reynolds numbers $Re = 3.2 \times 10^4 - 7.4 \times 10^4$ [11]. The authors used a low-speed wind tunnel to generate the flow and a hot wire probe and anemometer to measure the vortex-shedding frequencies of the upstream and downstream cylinder. Flow patterns for $P/D < 1.5$ were similar to those of a single cylinder in cross-flow, with both upstream and downstream cylinders having a similar shedding frequency. For $1.5 \leq P/D \leq 2.5$, the authors observed the presence of different Strouhal numbers for each cylinder when $\alpha > 30^\circ$. For $P/D > 2.5$, the authors measured the same Strouhal number for each cylinder for most α .

1.5 Objectives

The main objective of this thesis is to investigate how cylinder spacing, angle of flow incidence and Reynolds number affect the boundary layer separation of the downstream cylinder in a two-cylinder configuration. A low-speed open-circuit wind tunnel will be used to generate flows in the sub-critical regime and a hot film sensor will be used to measure vortex-shedding frequencies in the wake of the

downstream cylinder. Measurements performed by previous researchers will be repeated in order to determine if data obtained by these experiments can be corroborated utilizing the experimental configuration from this thesis. In addition, this thesis will investigate the presence of multi-modal vortex-shedding in the wake of the downstream cylinder at varying $P/D, \alpha, Re_D$.

2 Experimental Setup

2.1 Overview

Several items were designed and manufactured for this experiment. The circular cylinders used were cut to length from 1/2" Schedule 40 PVC. A special wind tunnel bottom hatch was laser cut from acrylic to allow the probe with the hot film sensor to be inserted into the test section of the wind tunnel from the bottom. A locking apparatus was also constructed from acrylic and mounted to this bottom hatch to fix the probe in place with a set screw during wind tunnel operation. Acrylic side plates were constructed to secure the cylinders in the wind tunnel test section. The side plates had several different countersunk holes machined to enable the cylinders to be fixed at different P/D spacings. The cylinders were press fit onto Delrin plugs at either end that were threaded to enable a fastening screw to secure the cylinders to the side plates. The cylinders could then be rotated about the axis passing through the parallel center-line between them by rotating the outside side plate, thus changing α . In this experiment, α was varied between 0 and 90° and P/D of 2, 3 and 4 were tested. In addition, measurements were taken for different Reynolds numbers in the high sub-critical regime by varying the drive frequency of the wind tunnel.

To measure the vortex-shedding frequency, a hot film sensor was inserted into the wake of the downstream cylinder in order to capture the periodic vortex detachment. A constant temperature anemometer was used to supply power to the hot film sensor and King's Law was used to convert the anemometer's output voltage into velocity.

2.2 Equipment Configuration

In this experiment, a low-speed open-circuit wind tunnel was used to generate the flow. This wind tunnel was manufactured by Engineering Laboratory Design Inc. and had a 0.6096 m x 0.6096 m test section (see Fig. 2.1). In addition, the wind tunnel was variable frequency drive which allowed the flow velocity to be adjusted easily.



Figure 2.1: Open-circuit wind tunnel used in this experiment.

Both cylinders used had diameter $D = 0.0213$ m and length $L = 0.6096$ m. The aspect ratio, $AR = L/D$, was therefore 28.62. The solid blockage ratio per cylinder in the wind tunnel test section was 3.5 %. This was the ratio of frontal cylinder area ($L \times D$) to test section area ($L \times L$). Depending on α , the maximum solid blockage ratio for both cylinders in the wind tunnel test section was 7.0 %. A single-component TSI 1201 hot film sensor and TSI 1750 constant temperature anemometer were used to measure vortex-shedding frequencies in the center of the wind tunnel behind the downstream cylinder (see Fig. 2.2). The hot film sensor was held in place by a TSI 1210 probe which was inserted into the test section from the bottom of the wind tunnel.

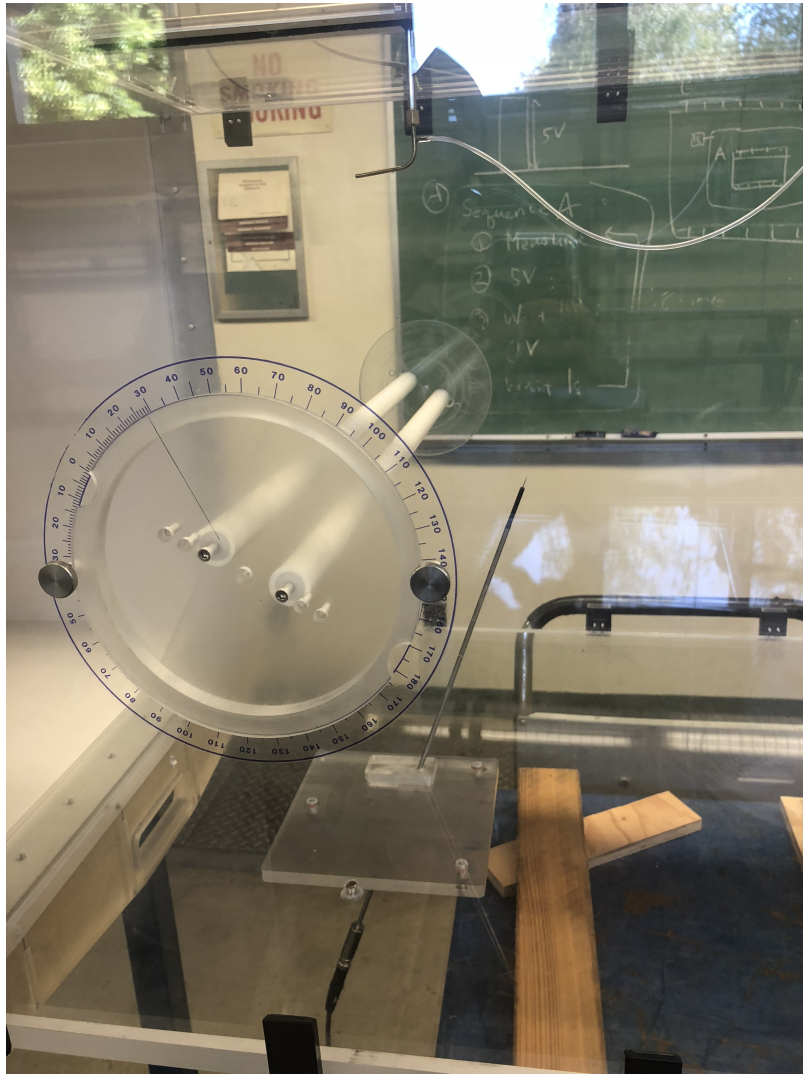


Figure 2.2: Side view of cylinder and probe configuration in wind tunnel test section with Pitot-static tube used to provide reference flow conditions (probe is angled rod sticking up from bottom of wind tunnel).

The film sensor was constructed from platinum film $50.8\ \mu\text{m}$ in diameter. A Pitot-static tube and Omega 163PC01D36 differential pressure transducer were utilized to provide reference flow velocities. Additionally, a BK Precision 2120B oscilloscope and Agilent 33210A function generator were used to verify the frequency response of the hot film sensor (see Appendix A). The DAQ system used to acquire voltage signals from the anemometer and pressure transducer consisted of a National Instruments SCXI-1180/1181 Feedthrough Panel, Breadboard Module and LabVIEW software. A full list of the equipment used in this experiment has been included in Appendix B.

2.3 Cylinder Configurations

The cylinder configuration nomenclature used in this experiment includes the pitch P , or center to center distance between cylinders, the angle α between the flow axis and the line connecting the cylinders, and the cylinder diameter D (see Fig. 2.3).

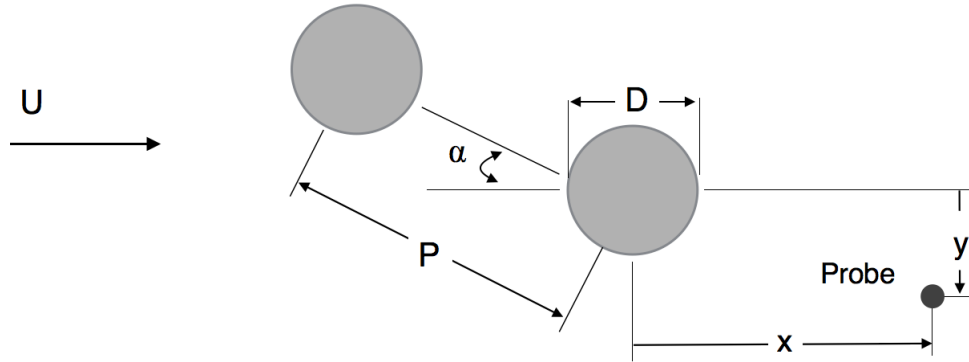


Figure 2.3: Schematic of cylinder and probe configuration in wind tunnel test section.

According to [5] and [6], the placement of a hot wire sensor is critical to obtaining accurate vortex-shedding frequency measurements. The probe with the hot film sensor fixed to the tip was placed at an approximate distance of $x/D = 5$ and $y/D = 1$ in order to capture the vortex-shedding frequency in the vortex street behind downstream cylinder [11].

2.4 Thermal Anemometer Calibration

Thermal anemometry is the use of an electrically heated probe (hot film sensor) to measure flow velocity. A constant temperature anemometer utilizes a Wheatstone bridge to supply power to the film sensor, which constitutes one of the 4 bridge resistances. Supplying electric current to the film sensor causes it to heat up due to the inherent electrical resistance of the sensor's material, this process is otherwise known as Joule heating. When subjected to a flow, the film sensor will cool due to convective heat transfer, thereby changing the resistance that the sensor contributes to the bridge and unbalancing it. An operational amplifier will then supply more power to the bridge in order to balance it and maintain a constant film sensor resistance and therefore constant temperature. By measuring the bridge voltage, the flow velocity can be determined [12]. King's Law relates the convective heat transfer from a conducting cylinder to the

electrical input power provided to the cylinder. Assuming negligible losses to conduction and radiation and that the cylinder has a high aspect ratio, King's Law can be used to compute the fluid velocity for an incompressible flow [12]. King's Law can be expressed as:

$$P = A + B(Re_D)^n, \quad (5)$$

where P is the electrical input power supplied to the cylinder and A , B and n are constants. The Reynolds number Re_D of the hot film sensor with fluid temperature at 20 ° C ($\nu = 1.52\text{e-}05 \text{ m}^2/\text{s}$) was:

$$Re_D = \frac{UD}{\nu} = 3.328 \left[\frac{\text{s}}{\text{m}} \right] U. \quad (6)$$

From Ohm's Law, power supplied to the hot film sensor P is proportional to the square of the voltage drop across the sensor divided by resistance: E^2/R . For the purposes of calibration, the resistance R of the hot film sensor was assumed to be constant and therefore the power supplied P was considered proportional to E^2 . This enabled King's Law to be expressed in terms of measurable quantities: ($B' = 3.328^n B$).

$$E^2 = A + B'(U)^n. \quad (7)$$

In order to calibrate the thermal anemometer, the constants in King's Law (see Eq. 7) had to be determined. This was done by measuring the output voltage from the anemometer for a variety of wind tunnel flow velocities. The reference flow velocities were provided by a Pitot-Static tube and an Omega 163PC01D36 Differential Pressure Transducer. A relationship was then made between anemometer output voltage and flow velocity.

The square of anemometer output voltage E^2 was plotted vs. flow velocity U^n for different values of n in order to determine the value of n that gave the highest correlation coefficient. The value of $n = 0.5$ was found to yield a correlation coefficient of $r = 0.9984$. The relationship between E^2 and U^n is plotted in Figure 2.4.

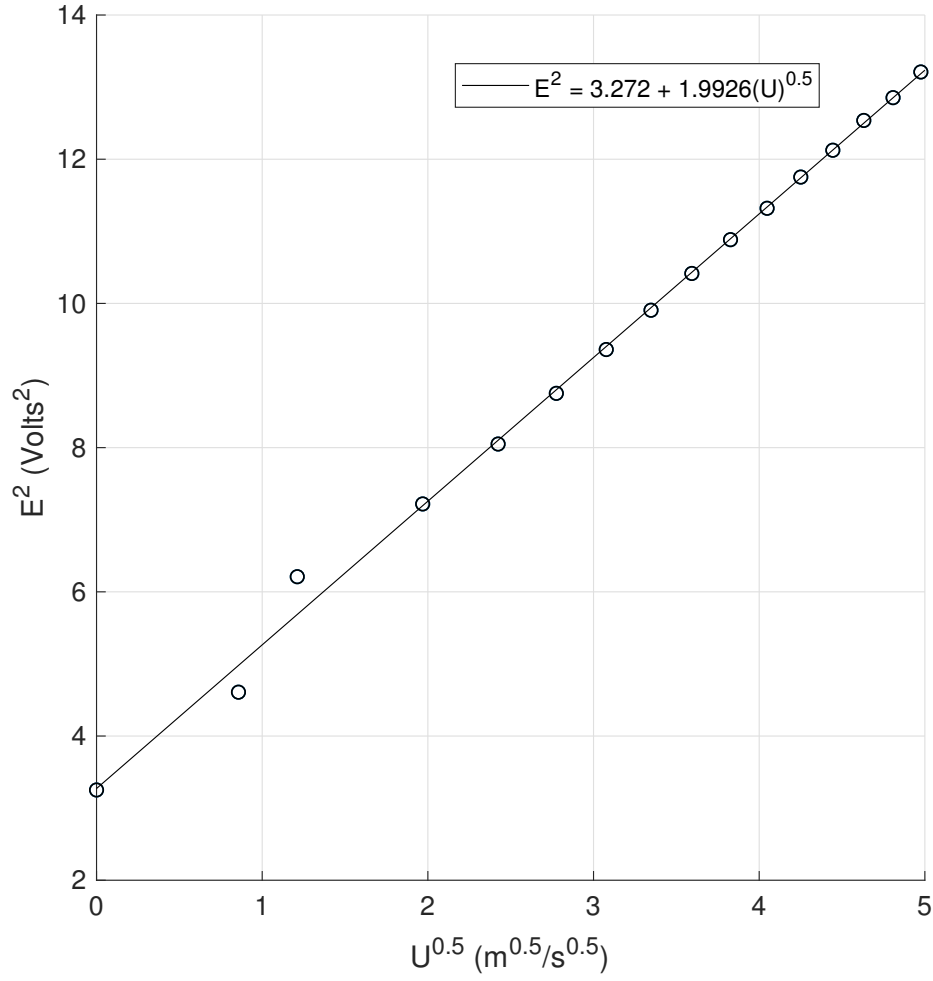


Figure 2.4: Constant temperature thermal anemometer calibration curve: correlation coefficient $r = 0.9984$.

Because Equation (7) is in slope-intercept form, constant A can be defined as the y-intercept and constant B' can be defined as the slope of a linear fit line to the relationship between E^2 and U^n plotted in Figure 2.4. This linear fit line yielded values for King's Law constants A and B' having units of $3.272 \text{ (V}^2\text{)}$ and $1.9926 \left(\frac{\text{V}^2}{\text{m}^{0.5}/\text{s}^{0.5}} \right)$ respectively. Substituting these values into King's Law gave:

$$E^2 = 3.272 + 1.9926(U)^{0.5}. \quad (8)$$

Solving Equation (8) yielded an expression for wind tunnel velocity U in terms of thermal anemometer voltage E :

$$U = \sqrt{\frac{E^2 - 3.272}{1.9926}} \quad (\text{m/s}). \quad (9)$$

The relationship established between E^2 and $U^{0.5}$ by this calibration procedure, evident by the high correlation coefficient, validated the assumption that the thermal anemometer system followed King's Law. With the exception of some deviation at low flow velocities, this relationship is accurately expressed by Equation (9). The deviation at low flow velocities was an experimental error attributed to the low signal to noise ratio resulting from the measurement equipment used.

2.5 Testing Procedure

The constant temperature anemometer and hot film sensor were used to measure vortex-shedding frequencies for various cylinder configurations. Measurements were taken for cylinder configurations ranging from $\alpha = 0 - 90^\circ$, P/D spacings of 2, 3 and 4, and $Re_D = 1.70\text{e}+04$, $2.89\text{e}+04$, and $3.98\text{e}+04$. Both cylinders were fixed to a circular side plate with degree markings on the outside of the wind tunnel's test section (see Fig. 2.5). The angle of flow incidence, α , was varied by rotating the side plate by hand from the outside of the wind tunnel. By rotating the side plate and aligning an angular indicator line printed on the outside of the plate, the cylinders were rotated to the desired angle of flow incidence.

After collecting preliminary data at α intervals every 5° , it became apparent that the Strouhal number varied predictably from $20 < \alpha \leq 90^\circ$. The relationship between St and α from $0 \leq \alpha \leq 20^\circ$ displayed much more interesting and complex behavior for $P/D = 2$ and 3. Therefore, subsequent St measurements were taken every 2° in this regime and every 10° for the predictable regime $20 < \alpha < 90^\circ$. For $P/D = 4$ and $Re_D = 1.70\text{e}+04$ and $Re_D = 3.98\text{e}+04$, measurements were only taken at select α since the trend was apparent (see Figs. C.8 and C.10). The list of measurements taken is included in Table 2.1 and observations of St behavior for different α and P/D spacing are summarized in Table 3.2.

Table 2.1: Flow incidence angles α for which St was measured.

	$P/D = 2$	$P/D = 3$	$P/D = 4$
$Re_D = 1.70\text{e}+04$	$\alpha = 0 - 20^\circ$, every 2° $\alpha = 20 - 90^\circ$, every 10°	$\alpha = 0 - 20^\circ$, every 2° $\alpha = 20 - 90^\circ$, every 10°	$\alpha = 0, 4, 10, 14, 20^\circ$ $\alpha = 30 - 90^\circ$, every 20°
$Re_D = 2.89\text{e}+04$	$\alpha = 0 - 20^\circ$, every 2° $\alpha = 20 - 90^\circ$, every 10°	$\alpha = 0 - 20^\circ$, every 2° $\alpha = 20 - 90^\circ$, every 10°	$\alpha = 0 - 20^\circ$, every 2° $\alpha = 20 - 90^\circ$, every 10°
$Re_D = 3.98\text{e}+04$	$\alpha = 0 - 20^\circ$, every 2° $\alpha = 20 - 90^\circ$, every 10°	$\alpha = 0 - 20^\circ$, every 2° $\alpha = 20 - 90^\circ$, every 10°	$\alpha = 0, 4, 10, 14, 20^\circ$ $\alpha = 30 - 90^\circ$, every 20°

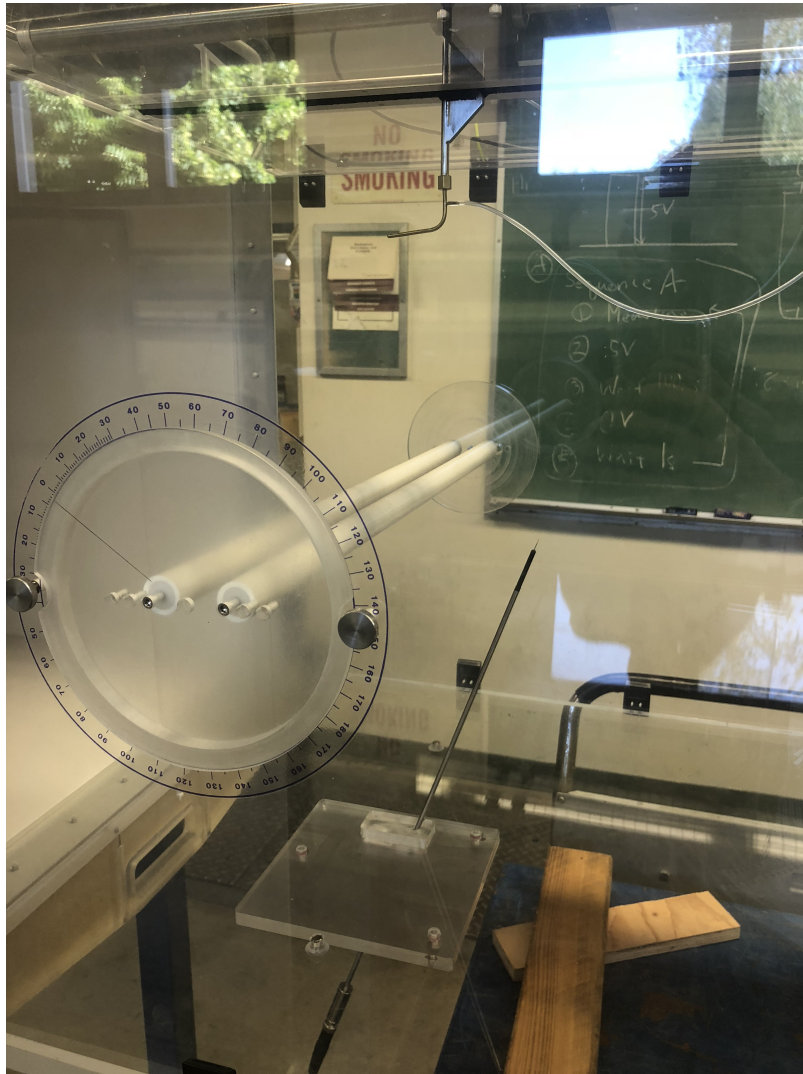


Figure 2.5: Close-up of the flow incidence adjusting plate.

The P/D cylinder spacing was varied by screwing the two cylinders into different sets of countersunk holes that were tapped into the circular side plate. A second side plate at the other wall of the wind tunnel's test section ensured cylinder rigidity and had identical hole placement. The Reynolds number based on cylinder diameter Re_D was varied by adjusting the wind tunnel's motor frequency.

3 Experimental Results

3.1 Strouhal Number Measurements

To measure the frequency of vortex-shedding f , the constant temperature anemometer's output voltage was acquired with the SCXI-1180/1181 in LabVIEW at 10 second intervals with a sampling frequency $F_s = 5000$ (Hz). This voltage was then converted into flow velocity using King's Law (see Equation (9)). To reduce signal noise, the mean velocity was subtracted from the signal. A Fast Fourier Transform (FFT) was then performed on the velocity signal in MatLab using Welch's method. Welch's method is a non-parametric method that utilizes FFT to estimate the power spectrum of a signal [13]. The "pwelch" function in MatLab was used to perform Welch's method on the velocity data. This process created a power spectrum of present frequencies in the signal. Each power spectrum presented in this thesis is the result of 5 averages. The dominant frequencies in the power spectrum were considered to be the dominant vortex-shedding frequencies. The Strouhal number was then calculated using Equation (2). Reported Strouhal numbers were not corrected for blockage ratio for the same reasons explained by Kiya et al. (1980).

3.2 Test Results

3.2.1 Time-synchronous Signal Averaging

Time-synchronous averaging enables a periodic waveform to be extracted from a noisy signal [14]. A time synchronous average was used to reconstruct the periodic velocity waveform associated with the dominant vortex-shedding frequency from the downstream cylinder. Utilizing the "tsa" function in MatLab, the velocity signal obtained with the constant temperature anemometer was broken down into segments. The "tsa" function then calculated the Discrete Fourier Transform for each segment and then averaged the power spectra from these segments. An Inverse Fourier Transform then converted the averaged signal back to the time domain. The sampling frequency and dominant vortex-shedding frequency were input into the MatLab "tsa" function. Time synchronous averages were plotted for various P/D , α , and Re_D for one period of revolution in the color blue, overlaid on the signal noise present (black). Figures 3.6, 3.8, and 3.10 represent a cylinder configuration with one strong vortex-shedding frequency. Figures 3.7, 3.9, and 3.11 represent a cylinder configuration with two predominant vortex-shedding frequencies, one of which is a scalar multiple of the other.

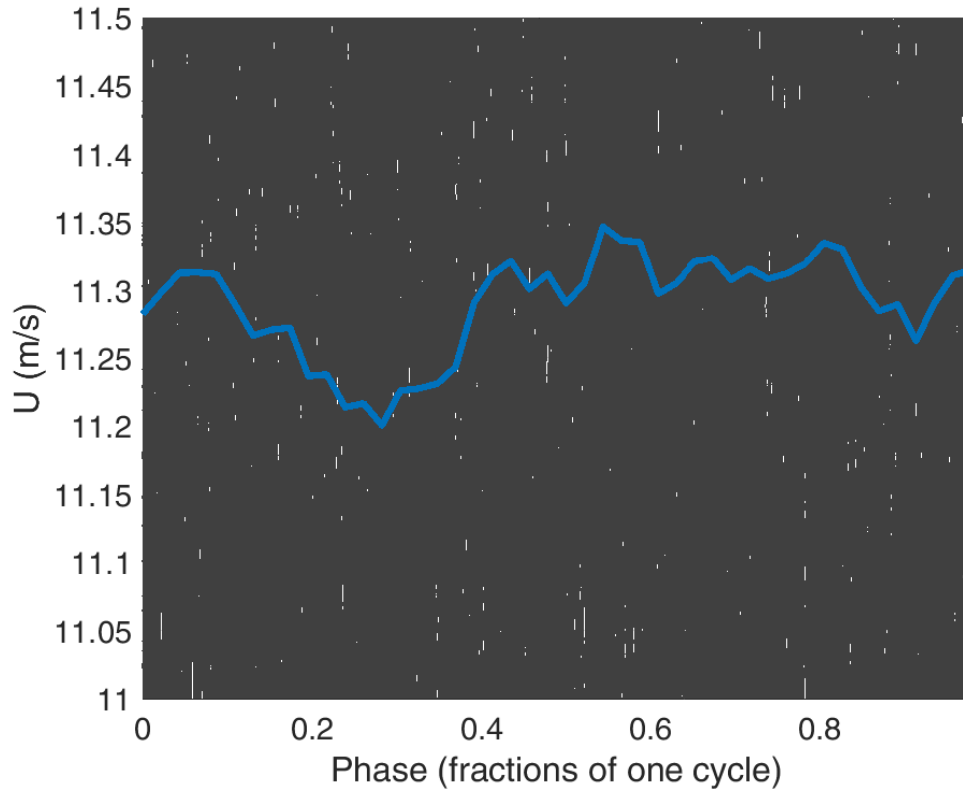


Figure 3.6: Time-synchronous signal average (blue) for $P/D = 2$, $\alpha = 90^\circ$: $Re_D = 1.70e+04$, overlaid on signal noise (black). Velocity waveform is plotted for one period of oscillation.

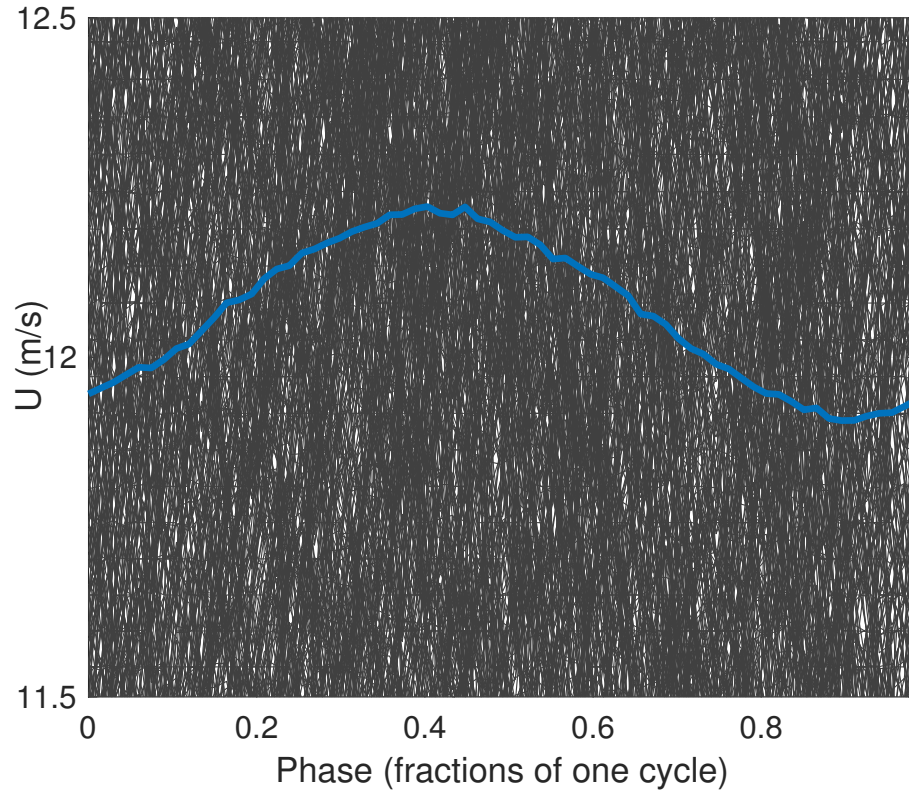


Figure 3.7: Time-synchronous signal average (blue) for $P/D = 2$, $\alpha = 30^\circ$: $Re_D = 1.70e+04$, overlaid on signal noise (black). Velocity waveform is plotted for one period of oscillation.

The time-synchronous average for $P/D = 2$, $\alpha = 90^\circ$: $Re_D = 1.70e+04$ in Figure 3.6 extracted a signal that appears far from a perfect sinusoid. This is in contrast to the signal in Figure 3.7, which appears to be much closer to sinusoidal. A signal closer to a sinusoidal indicates more regular vortex-shedding events. A more irregular signal indicates higher frequency shedding variation or more aperiodic vortex-shedding events.

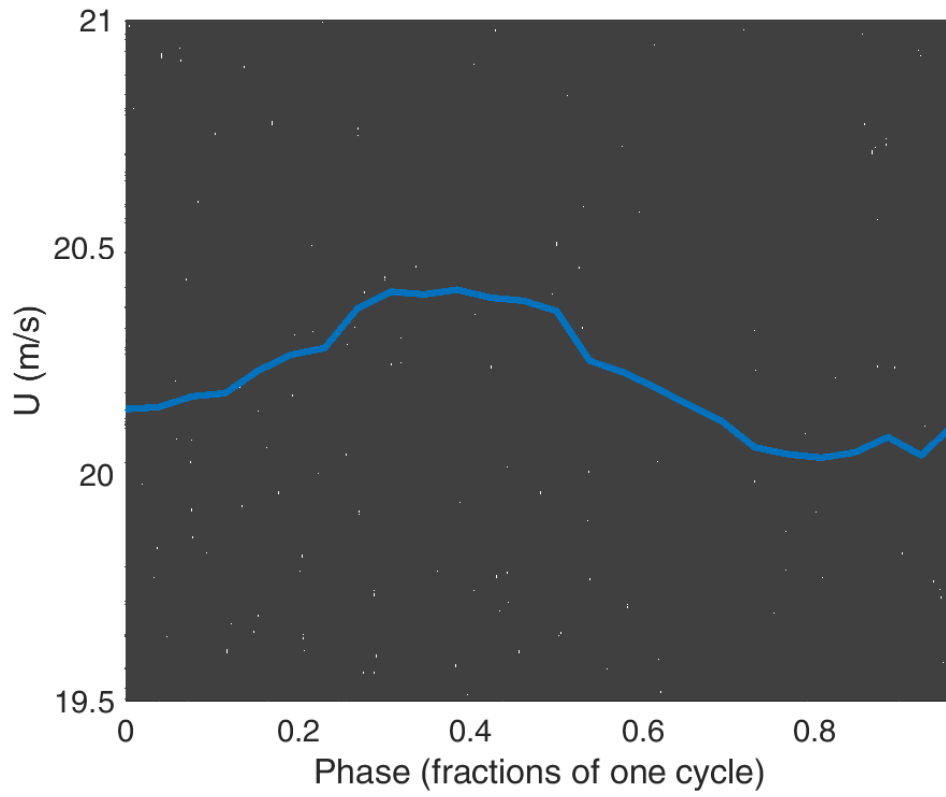


Figure 3.8: Time-synchronous signal average (blue) for $P/D = 2$, $\alpha = 90^\circ$: $Re_D = 2.89e+04$, overlaid on signal noise (black). Velocity waveform is plotted for one period of oscillation.

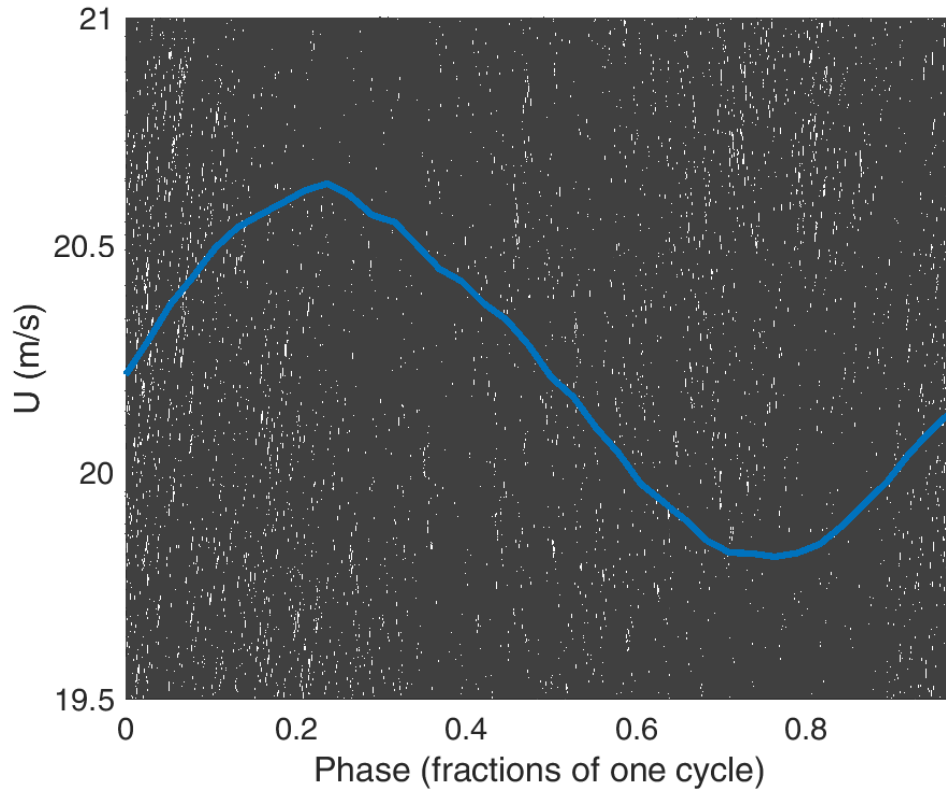


Figure 3.9: Time-synchronous signal average (blue) for $P/D = 2$, $\alpha = 30^\circ$: $Re_D = 2.89e+04$, overlaid on signal noise (black). Velocity waveform is plotted for one period of oscillation.

The time-synchronous average for $P/D = 2$, $\alpha = 90^\circ$: $Re_D = 2.89e+04$ in Figure 3.8 is nearly sinusoidal in appearance and the signal extracted in Figure 3.9 for $\alpha = 30^\circ$ is closest to a sinusoid.

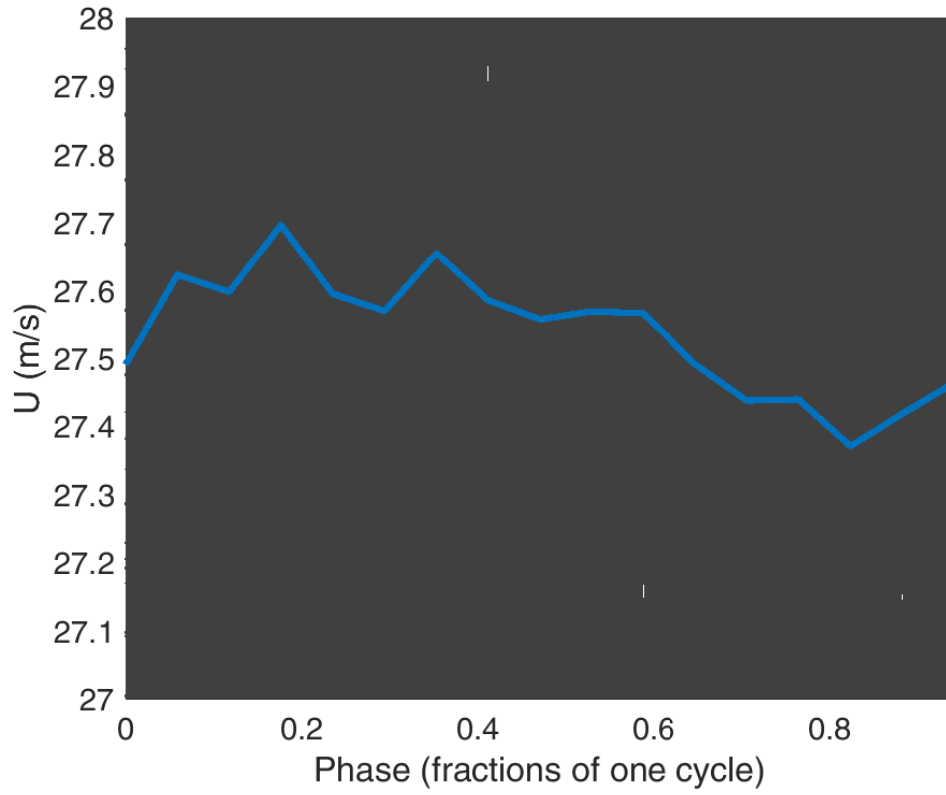


Figure 3.10: Time-synchronous signal average (blue) for $P/D = 2$, $\alpha = 90^\circ$: $Re_D = 3.98e+04$, overlaid on signal noise (black). Velocity waveform is plotted for one period of oscillation.

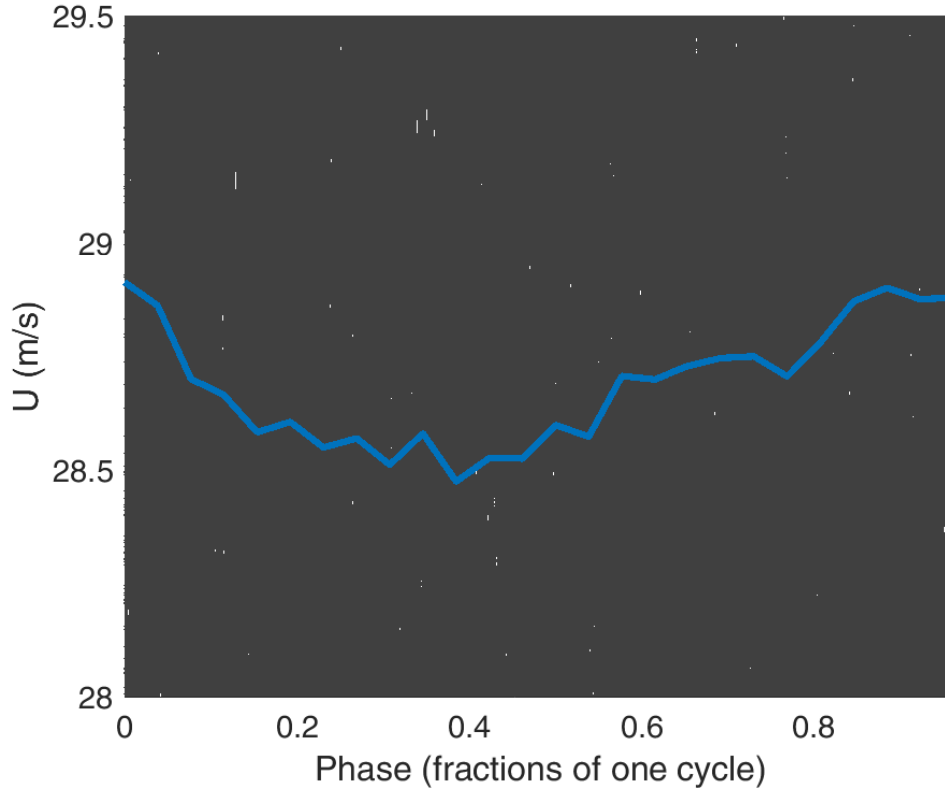


Figure 3.11: Time-synchronous signal average (blue) for $P/D = 2$, $\alpha = 30^\circ$: $Re_D = 3.98e+04$, overlaid on signal noise (black). Velocity waveform is plotted for one period of oscillation.

Both time-synchronous averages for $P/D = 2$, $\alpha = 90^\circ$: $Re_D = 3.98e+04$ in Figures 3.10 and 3.11 appear to be only vaguely sinusoidal.

Those extracted velocity signals with strong sinusoidal appearance correspond to cylinder configurations and Reynolds numbers with strong vortex-shedding frequency peaks in the power spectra. The extracted velocity signals without sinusoidal appearance are associated with cylinder configurations having weak or broad peaks in the power spectra.

3.2.2 Strouhal Number Data

Power spectra were obtained using the process outlined in Section 3.1 for cylinder configurations ranging from $0 \leq \alpha \leq 90^\circ$, P/D spacings of 2, 3 and 4, and $Re_D = 1.70e+04$, $2.89e+04$, and $3.98e+04$. These power spectra are located in Appendix C, (see Figures C.2 - C.10). The same MatLab program used to

create these power spectra was also utilized to locate the Strouhal numbers at each power spectrum's peaks. The relationship between St , α , Re_D and P/D is displayed in Figures 3.14 - 3.16. Various cylinder configurations had two predominant vortex-shedding frequencies, one of which was exactly twice as large as the other. This is called frequency doubling and indicates that the oscillating velocity signal was not an exact sine wave, as evidenced by the discussion in 3.2.1 (performing time-synchronous signal averages signals indicated that the velocity signals obtained in the downstream cylinder's wake were periodic but not perfectly sinusoidal). The Strouhal number associated with the lower vortex-shedding frequency is referred to as the first mode and the Strouhal number associated with the higher vortex-shedding frequency is referred to as the second mode. Both first and second modes of vortex-shedding are in-phase. On occasion, three vortex-shedding frequencies were present. When there were three modes and the first and third were integer multiples of each other, the second mode in between represented out-of-phase vortex-shedding.

Three predominant vortex-shedding frequencies were present for select configurations. When a third mode was present, the St for that mode was nearly twice the magnitude of the first mode and the St of second mode was somewhere in between. Figures 3.12 and 3.13 are select power spectra taken from the experimental data set in Appendix C. The Strouhal numbers indicated in these power spectra and the rest of the experimental data set are plotted vs. α for different P/D and Re_D in Figures 3.14 - 3.16.

In Figures 3.12, 3.13, and in several power spectra in Appendix C, there exist labeled peaks which are broad-banded or non-existent. This indicates a weak signal and a weak or inconsistent vortex-shedding process [11]. For $P/D = 3$ and $Re_D = 2.89e+04$, weaker vortex-shedding occurred from $2 \leq \alpha < 12^\circ$ and $60 \leq \alpha \leq 90^\circ$. For $P/D = 4$ and $Re_D = 1.70e+04$, weaker vortex-shedding occurred at $\alpha = 0^\circ$. Conversely, sharp, easily recognizable peaks indicate strong vortex-shedding.

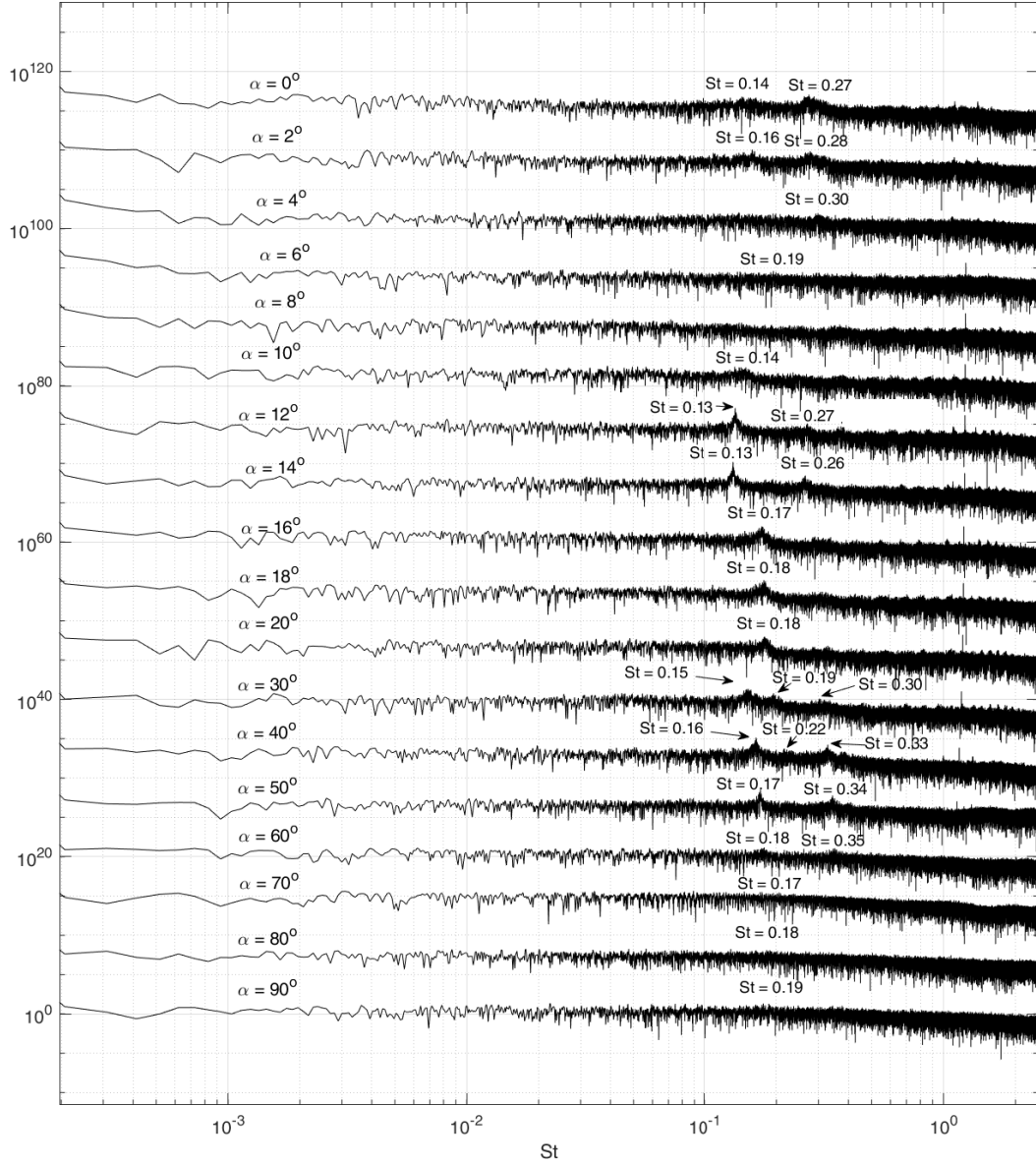


Figure 3.12: St vs. α for $P/D = 3$: $Re_D = 2.89e+04$. Each power spectrum has been shifted up 10^7 from the previous power spectrum in order to present them all on the same plot. In addition, each power spectrum is the result of 5 averages.

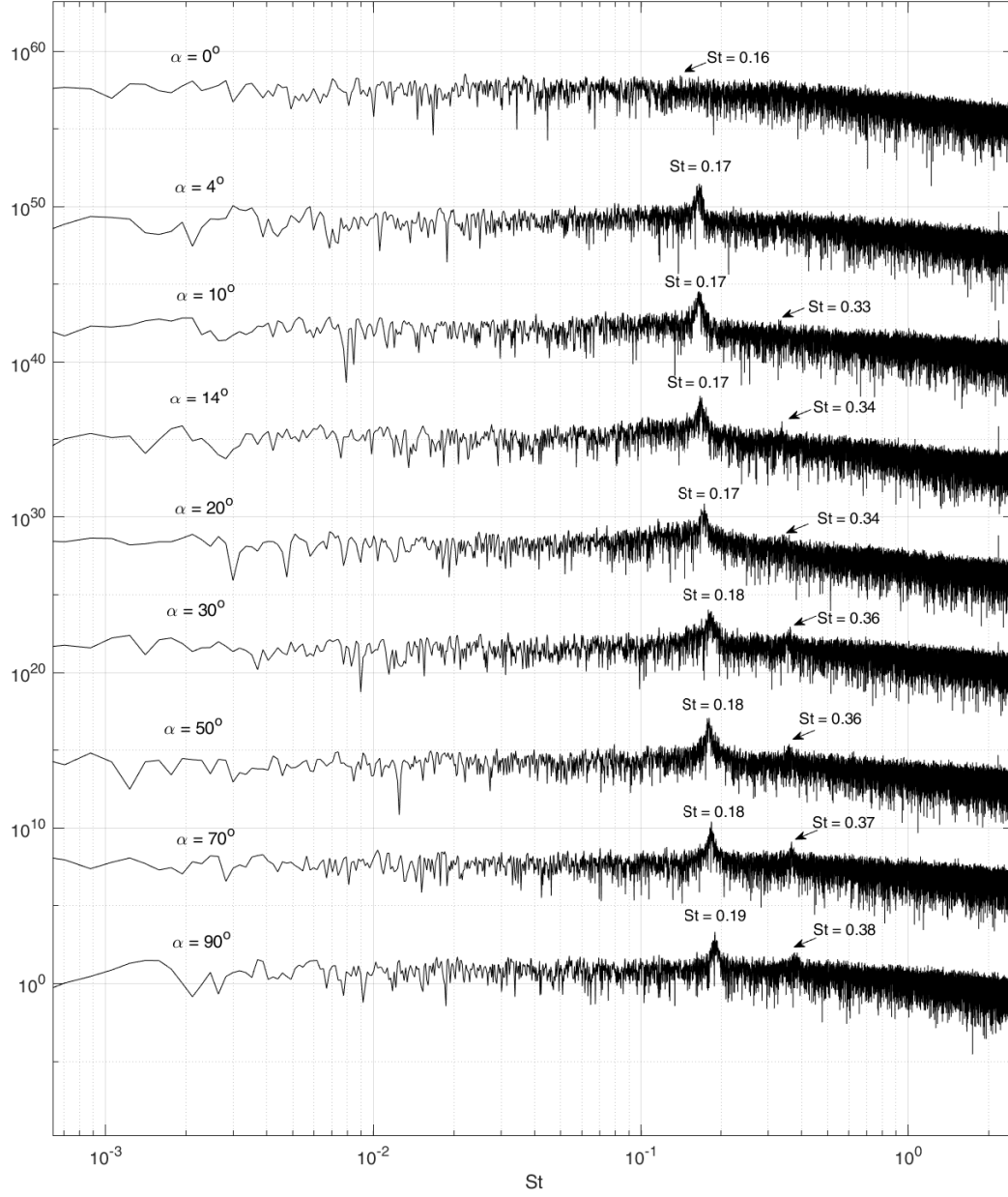


Figure 3.13: St vs. α for $P/D = 4$: $Re_D = 1.70e+04$. Each power spectrum has been shifted up 10^7 from the previous power spectrum in order to present them all on the same plot. In addition, each power spectrum is the result of 5 averages.

In Figures 3.12, 3.13 and those in Appendix C, the power spectra peaks were found with MatLab, confirmed with visual inspection and labeled. For power spectra of cylinder configurations with weaker vortex-shedding, the attempt to plot all flow incidence angles α in the same figure further broadened the peaks, making them more difficult to visually locate. To find these broad-banded peaks, the peaks were located with MatLab and visually confirmed by plotting each individual power spectrum alone for increased resolution. Occasionally, a peak could not be found using these methods, for example $P/D = 3$, $Re_D = 2.89e+04$ and $\alpha = 8^\circ$ (see Fig. 3.12). In these instances the vortex-shedding was considered to be extremely weak or non-existent.

Table 3.2: St vs. α observations.

	$P/D = 2$	$P/D = 3$	$P/D = 4$
$\alpha = 0 - 4^\circ$	St increasing rapidly	St increasing rapidly	St increasing moderately
$\alpha \approx 6 - 8^\circ$	Peak St value	Large St value w/ weak signal	St increasing moderately
$\alpha = 10 - 20^\circ$	St decreasing	Inconsistent trend	St increasing moderately
$\alpha = 20 - 90^\circ$	St increasing moderately	St increasing moderately	St increasing moderately

The relationship between Strouhal number, α and Re_D is plotted for $P/D = 2, 3, 4$ in Figures 3.14 - 3.16 respectively.

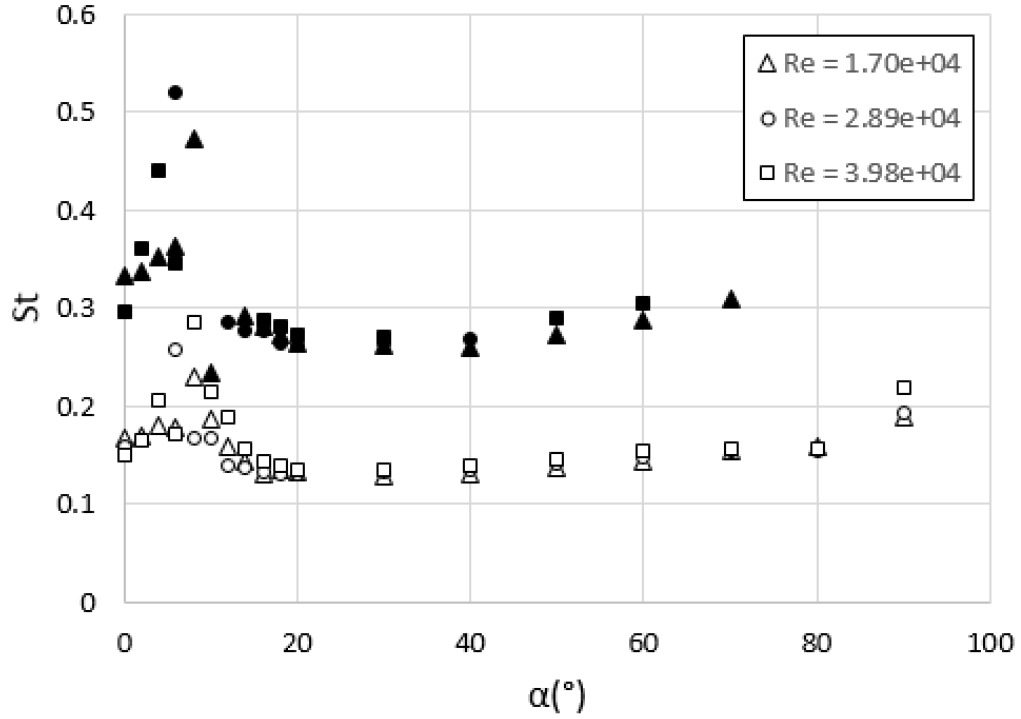


Figure 3.14: St vs. α for $P/D = 2$: 1st mode (\triangle , \circ , \square), 2nd/3rd mode (\blacktriangle , \bullet , \blacksquare).

In Figure 3.14, the Strouhal number for $P/D = 2$ can be seen to rapidly increase at low α . For $Re_D = 1.70e+04$, the 1st mode reached a maximum value of $St = 0.23$ at $\alpha = 8^\circ$. For $Re_D = 2.89e+04$, the 1st mode reached a maximum value $St = 0.26$ at $\alpha = 6^\circ$. For $Re_D = 3.98e+04$, the first mode reached a maximum value of $St = 0.27$ at $\alpha = 8^\circ$. The presence of a large Strouhal number at critical flow incidence angle $\alpha \approx 6 - 8^\circ$ is in agreement with Sumner et al. (2003) and (2008). After reaching a maximum value, the Strouhal number decreased until leveling out at $\alpha = 20^\circ$. St then increased moderately from $20 < \alpha \leq 90^\circ$ towards the single cylinder value. For $P/D = 2$ spacing a strong 2nd mode peak was present from $\alpha = 0^\circ - 6^\circ$ and $\alpha = 16^\circ - 30^\circ$ for all three Reynolds numbers tested. Smaller 2nd mode peaks were present at higher α . The behavior of St approaching the single cylinder value as α increased is in accordance with Kiya et al. (1980) and Sumner et al. (2008). Overall, the relationship between α and St was similar for all three Reynolds numbers, with all three data sets increasing and decreasing for similar ranges of α .

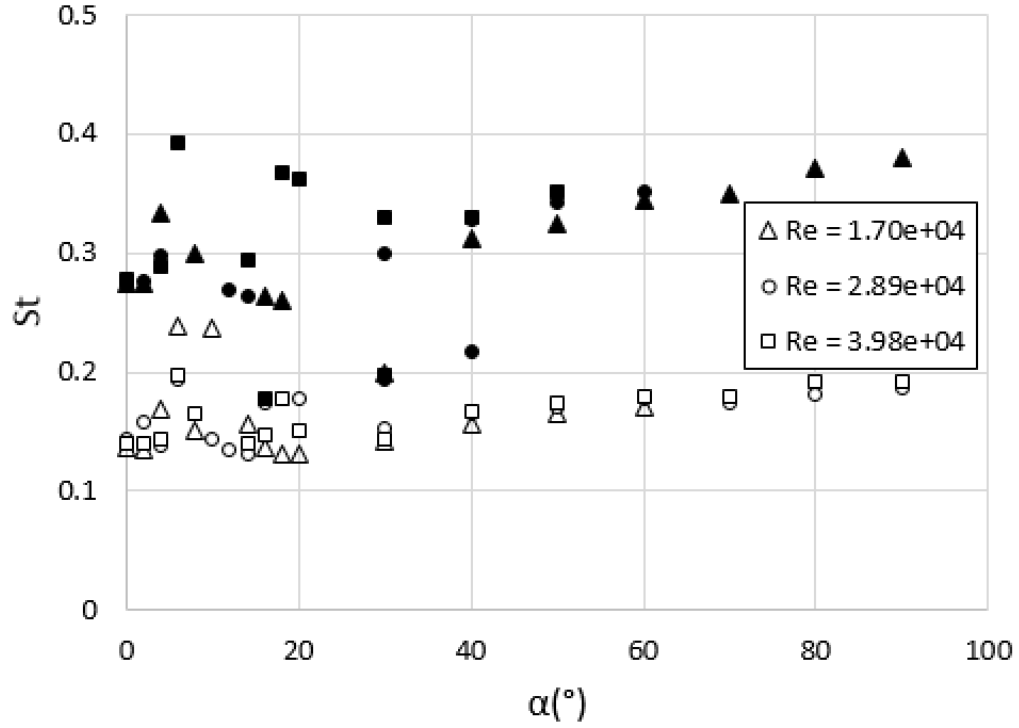


Figure 3.15: St vs. α for $P/D = 3$: 1st mode (\triangle , \circ , \square), 2nd/3rd mode (\blacktriangle , \bullet , \blacksquare).

In Figure 3.15, the Strouhal number for $P/D = 3$ also increased rapidly at low α , however the trend was not as clean as for the $P/D = 2$ spacing. For $Re_D = 1.70e+04$, the 1st mode reached a maximum value of $St = 0.24$ at $\alpha = 6^\circ$, then two modes were present at $\alpha = 8^\circ$, and only the 1st mode $St = 0.24$ was present at $\alpha = 10^\circ$. For $Re_D = 2.89e+04$, the 1st mode reached a maximum value of $St = 0.30$ at $\alpha = 4^\circ$, then decreased to $St = 0.19$ at $\alpha = 6^\circ$, and no Strouhal number was present at $\alpha = 8^\circ$. For $Re_D = 3.98e+04$, the 1st mode reached a maximum value of $St = 0.20$ at $\alpha = 6^\circ$ with a 2nd mode $St = 0.39$, then decreased to $St = 0.17$ at $\alpha = 8^\circ$. No Strouhal number was present for $\alpha = 10^\circ$ or $\alpha = 12^\circ$. After reaching a maximum value, the Strouhal number decreased, increased then decreased before increasing with a consistent trend towards the single cylinder value. For $Re_D = 1.70e+04$, this trend was established at $\alpha = 18^\circ$. For $Re_D = 2.89e+04$ and $Re_D = 3.98e+04$ the Strouhal number did not increase monotonically until $\alpha = 30^\circ$. For $P/D = 3$ the presence of a strong 2nd mode generally followed the same pattern as the $P/D = 2$ configuration. Two modes were present at low α and reappeared by $\alpha = 30^\circ$ for all three Re_D , and from $\alpha = 70 - 90^\circ$, only the 2nd mode of St was detected. $P/D = 3$ was however, the only spacing to have a 3rd mode of vortex-shedding present in some of the power spectra. This 3rd mode occurred at $\alpha = 30^\circ$ for $Re_D = 1.70e+04$, $\alpha = 30^\circ$ and 40° for $Re_D = 2.89e+04$, and $\alpha = 30^\circ$ for $Re_D = 3.98e+04$. While there was

much more confusion in the St trend at lower α , the relationship between $\alpha > 30^\circ$ and St was similar for all three Reynolds numbers.

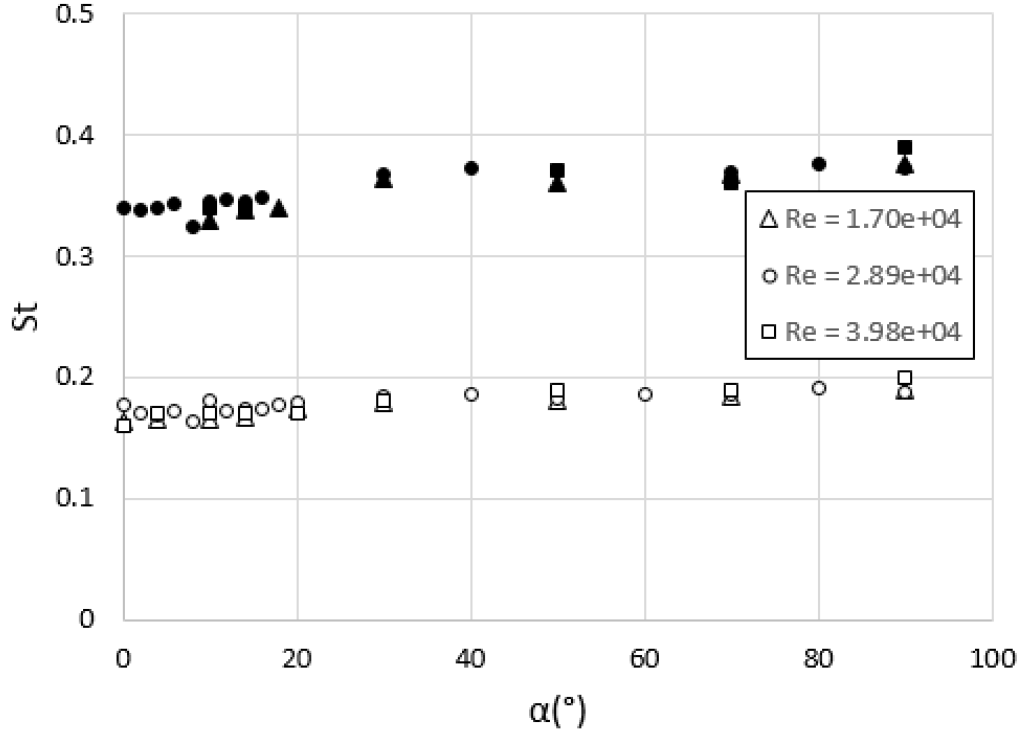


Figure 3.16: St vs. α for $P/D = 4$: 1st mode (Δ , \circ , \square), 2nd/3rd mode (\blacktriangle , \bullet , \blacksquare).

In Figure 3.16, the Strouhal number for $P/D = 4$ can be seen to increase moderately with α . Unlike $P/D = 2$ and 3, the $P/D = 4$ spacing does not have a peak St value near $\alpha = 8^\circ$ and instead monotonically increases from $\alpha = 0 - 90^\circ$ for all three Reynolds numbers tested. In addition, the 2nd mode was present more often than for $P/D = 2$ and 3. The stable behavior of vortex-shedding with respect to α for $P/D = 4$ and the fact that Strouhal numbers for all α were close to the single cylinder value of 0.2, indicated that the upstream cylinder had negligible effects on vortex-shedding of the downstream cylinder. This behavior is consistent with that found by Kiya et al. (1980) and Sumner et al. (2008).

The many cylinder configurations tested displayed various trends between the Strouhal number and increasing Reynolds number. For tandem cylinder arrangements ($\alpha = 0^\circ$), St decreased with increasing Re_D for $P/D = 2$, this concurred with Zhou et al. (2004). For $P/D = 3$ and 4, St increased slightly from $Re_D = 1.70e+04$ to $Re_D = 2.89e+04$ and decreased from $Re_D = 2.89e+04$ to $Re_D = 3.98e+04$ this differed

from the trend predicted by Zhou et al. (2004). For side by side cylinder arrangements ($\alpha = 90^\circ$), St increased with increasing Re_D for $P/D = 2$. For $P/D = 3$ and $Re_D = 1.70e+04$, the 1st mode Strouhal number was not detected, but St increased from $Re_D = 2.89e+04$ to $Re_D = 3.98e+04$. For $P/D = 4$, St decreased from $Re_D = 1.70e+04$ to $Re_D = 2.89e+04$ and increased from $Re_D = 2.89e+04$ to $Re_D = 3.98e+04$. No discernible trend between St and Re_D was observed from $0 < \alpha < 20^\circ$ for $P/D = 2, 3$ or 4 . Additionally, there was no clear correlation between the location of peak St for $P/D = 2$ and 3 and Reynolds number Re_D . From $20 < \alpha < 90^\circ$, St generally increased for all P/D with increasing Re_D .

4 Conclusion

Strouhal numbers from the downstream cylinder in a two infinite cylinder configuration were measured experimentally. The cylinders were of equal diameter and placed in cross-flow in a wind tunnel. St measurements were taken for different α , the angle between cylinders relative to the flow axis, and different P/D (dimensionless cylinder pitch) spacing. In this experiment, α was varied between 0 and 90° and P/D of 2, 3 and 4 were tested. In addition, measurements were taken for different Reynolds numbers in the high sub-critical regime.

Strouhal numbers varied considerably with α for P/D spacings of 2 and 3 in the low alpha range $\alpha = 0 - 20^\circ$, indicating a strong influence of the upstream cylinder on the downstream cylinder's vortex-shedding. For $P/D = 2$ and 3, St increased rapidly from $0 < \alpha < 4^\circ$ and at $\alpha \approx 6 - 8^\circ$, St reached a peak value. St decreased for $P/D = 2$ in the range of $10 < \alpha < 20^\circ$ and increased towards the single cylinder value of 0.2 from $20 < \alpha < 90^\circ$. St for $P/D = 3$ did not decrease monotonically after reaching a peak value at $\alpha \approx 6 - 8^\circ$ like $P/D = 2$, but similar to the $P/D = 2$ spacing, St increased towards the single cylinder value from $20 < \alpha < 90^\circ$. For $P/D = 4$, Strouhal numbers increased monotonically from $\alpha = 0 - 90^\circ$ for all three Reynolds numbers tested, but were never far from the single cylinder value, indicating that the larger spacing between cylinders reduced the vortex-shedding interference.

The Reynolds number was shown to have only a small effect on Strouhal number in this experiment, perhaps due to the relatively small range of Re_D tested. No discernible trend between St and Re_D was observed from $0 < \alpha < 20^\circ$ for $P/D = 2, 3$ or 4. Additionally, there was no clear correlation between the location of peak St for $P/D = 2$ and 3 and Reynolds number Re_D . However, Strouhal numbers in the range $20 < \alpha < 90^\circ$ generally increased for all P/D with increasing Re_D .

A large number of P/D and α configurations displayed frequency doubling where two dominant vortex-shedding frequencies were measured, one of which being twice as large as the other. This indicated that the velocity signal obtained in the wake of the downstream cylinder was not an exact sine wave, which was confirmed by performing time-synchronous signal averaging. The presence of two modal frequencies represented in-phase vortex-shedding. Three vortex-shedding frequencies were measured on rare occasion. When there were three modes and the first and third were integer multiples of each other, the second mode in between represented vortex-shedding that was out-of-phase from the other two modes. The presence of a second mode of vortex-shedding was observed at a large number of P/D and α cylin-

der configurations, and the rare occurrence of a 3rd mode of vortex-shedding was found at $\alpha = 30$ and 40° for $P/D = 3$.

References

- [1] Zdravkovich, M.M., (1977). Review of flow interference between two circular cylinders in various arrangements. *Journal of Fluids Engineering*, **99**, 618-631.
- [2] Tritton, D.J., (1998). "Physical Fluid Dynamics." 2nd ed., Oxford.
- [3] Kundu, P. K., and Cohen, I. M. (2008). "Fluid mechanics." 6th ed., Elsevier, New York.
- [4] Zdravkovich, MM., (1987). The effects of interference between circular cylinders in cross flow. *Journal of Fluids and Structures* **1**, 239-261.
- [5] Kiya, M., Arie, M., Tamura, H., and Mori, H., (1980). Vortex shedding from two circular cylinders in staggered arrangement. *ASME Journal of Fluids Engineering*, **102**, 166–173.
- [6] Sumner, D., Price, S.J., and Paidoussis, M.P., (2000). Flow-pattern identification for two staggered circular cylinders in cross-flow. *Journal of Fluid Mechanics*, **411**, 263–303.
- [7] Xu, G., and Zhou, Y., (2004). Strouhal numbers in the wake of two inline cylinders. *Experiments in Fluids*, **37**, 248–256.
- [8] Roshko, A. 1955 On the wake and drag of bluff bodies. *Journal of Aeronautical Science*, **22**, 124—132.
- [9] Williamson, C.H.K., and Brown, G.L., (1998). A series in $1/Re^{1/2}$ to represent the Strouhal–Reynolds number relationship of the cylinder wake. *Journal of Fluids and Structures*, **12**, 1073–1085.
- [10] Alam, M.M., and Zhou, Y., (2008). Strouhal numbers, forces and flow structures around two tandem cylinders of different diameters. *Journal of Fluids and Structures*, **24**, 505–526.
- [11] Sumner, D., Richards, M.D., and Akosile, O.O., (2008). Strouhal number data for two staggered circular cylinders. *Journal of Wind Engineering and Industrial Aerodynamics* **96**, 859–871.
- [12] Goldstein, J.R., (1996). "Fluid Mechanics Measurements." 2nd ed., Taylor and Francis, Washington DC.
- [13] Welch, P. D., (1967). The use of Fast Fourier Transform for the estimation of power spectra: A method based on time averaging over short, modified periodograms. *IEEE Transactions on Audio and Electroacoustics*, **15**, 70–73.

- [14] Bechhoefer, Eric, and Michael Kingsley, (2009). "A Review of Time-Synchronous Average Algorithms." Proceedings of the Annual Conference of the Prognostics and Health Management Society, San Diego, CA, September-October.

Appendices

A Frequency Response of Thermal Anemometer

To check the frequency response of the thermal anemometer, a square wave was sent into the anemometer's bridge. A 50 K Ω resistor was connected in series to a function generator supplying a 300 mV, 1 kHz square wave. For the hot film sensors used, the expected frequency response was $f = 1/t$, where t is the pulse width. The frequency response was measured by an oscilloscope to be 100 kHz (see Fig. A.1).

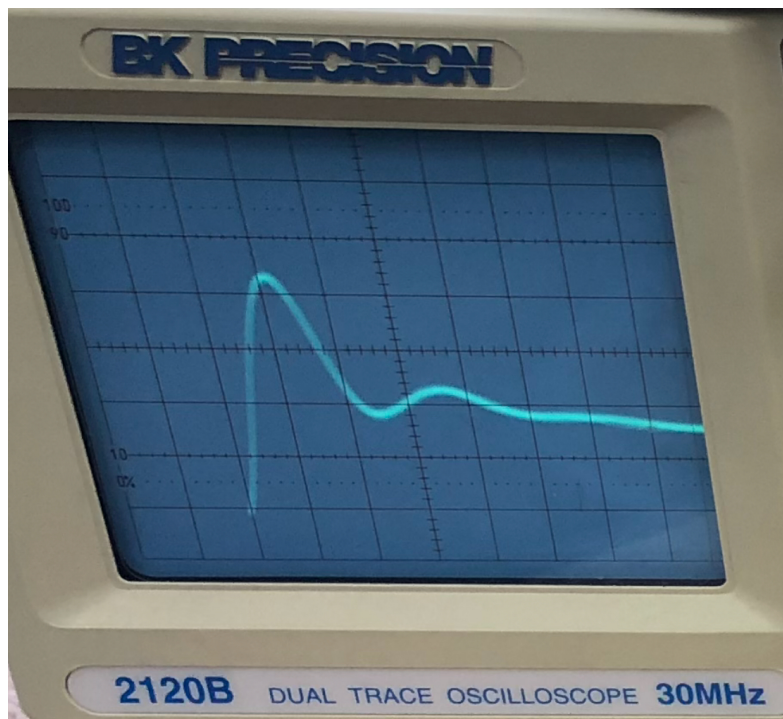


Figure A.1: Frequency response of hot film sensor, oscilloscope settings: 5 μ s/DIV, 0.1 mV/DIV.

B Experimental Equipment

- Constant Temperature Anemometer: TSI Model 1750
- Power Supply for Model 1750: TSI Model 1751
- DAQ: National Instruments SCXI-1180/1181 Feedthrough Panel and Breadboard Module
- Hot Film Sensors: TSI Model 1201
- Probe: TSI Model 1210
- 49 Ω Control Resistor: TSI Model 1304
- Oscilloscope: BK Precision 2120B
- Function Generator: Agilent 33210A
- 50 K Ω Resistor
- Cables & Adapters
- Omega 163PC01D36 Differential Pressure Transducer
- Pitot-Static Tube
- 24" Low-speed open-circuit wind tunnel: Engineering Laboratory Design Inc.

C Power Spectra

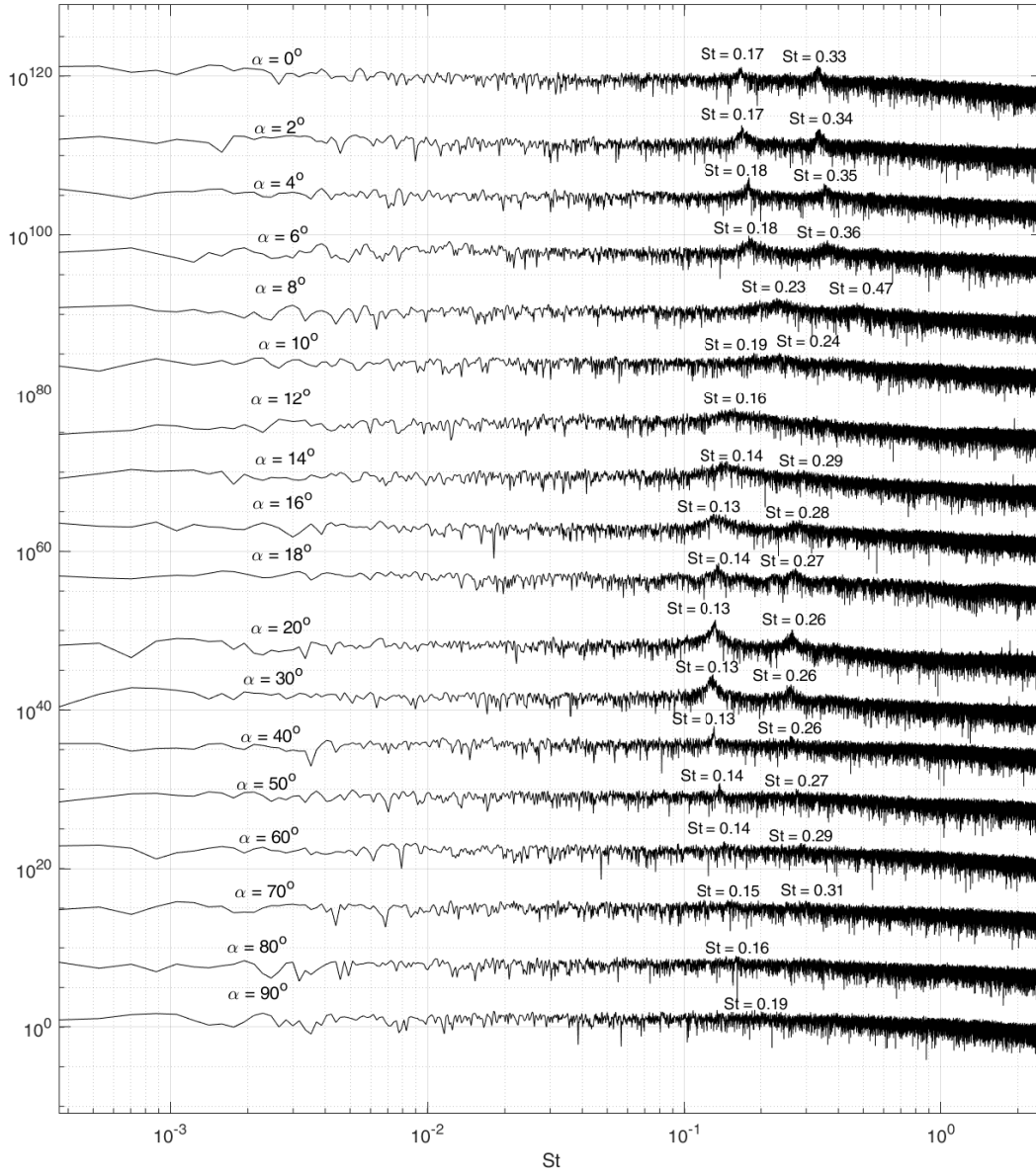


Figure C.2: St vs. α for $P/D = 2$: $Re_D = 1.70e+04$. Each power spectrum is the result of 5 averages.

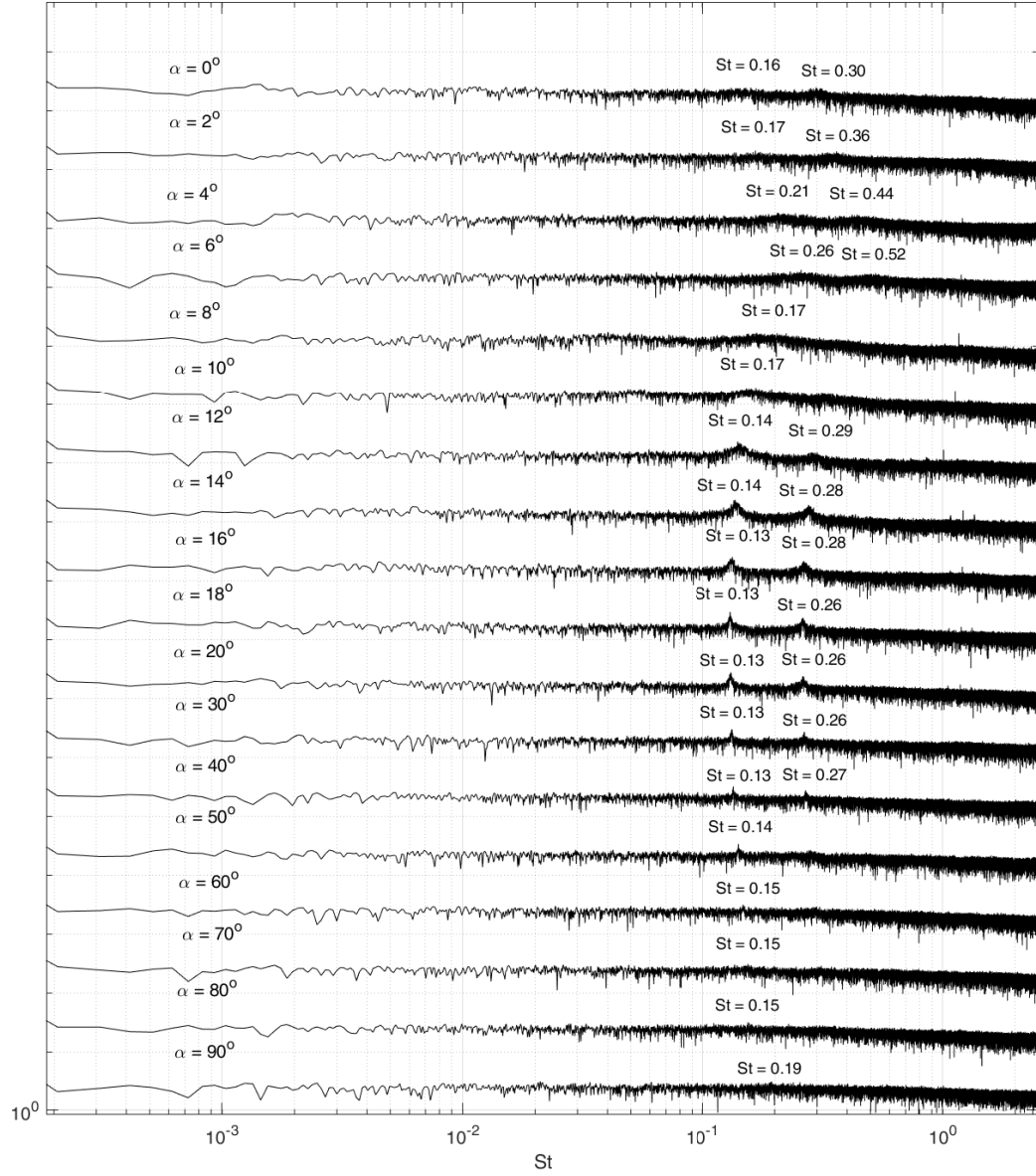


Figure C.3: St vs. α for $P/D = 2$: $Re_D = 2.89e+04$. Each power spectrum is the result of 5 averages.

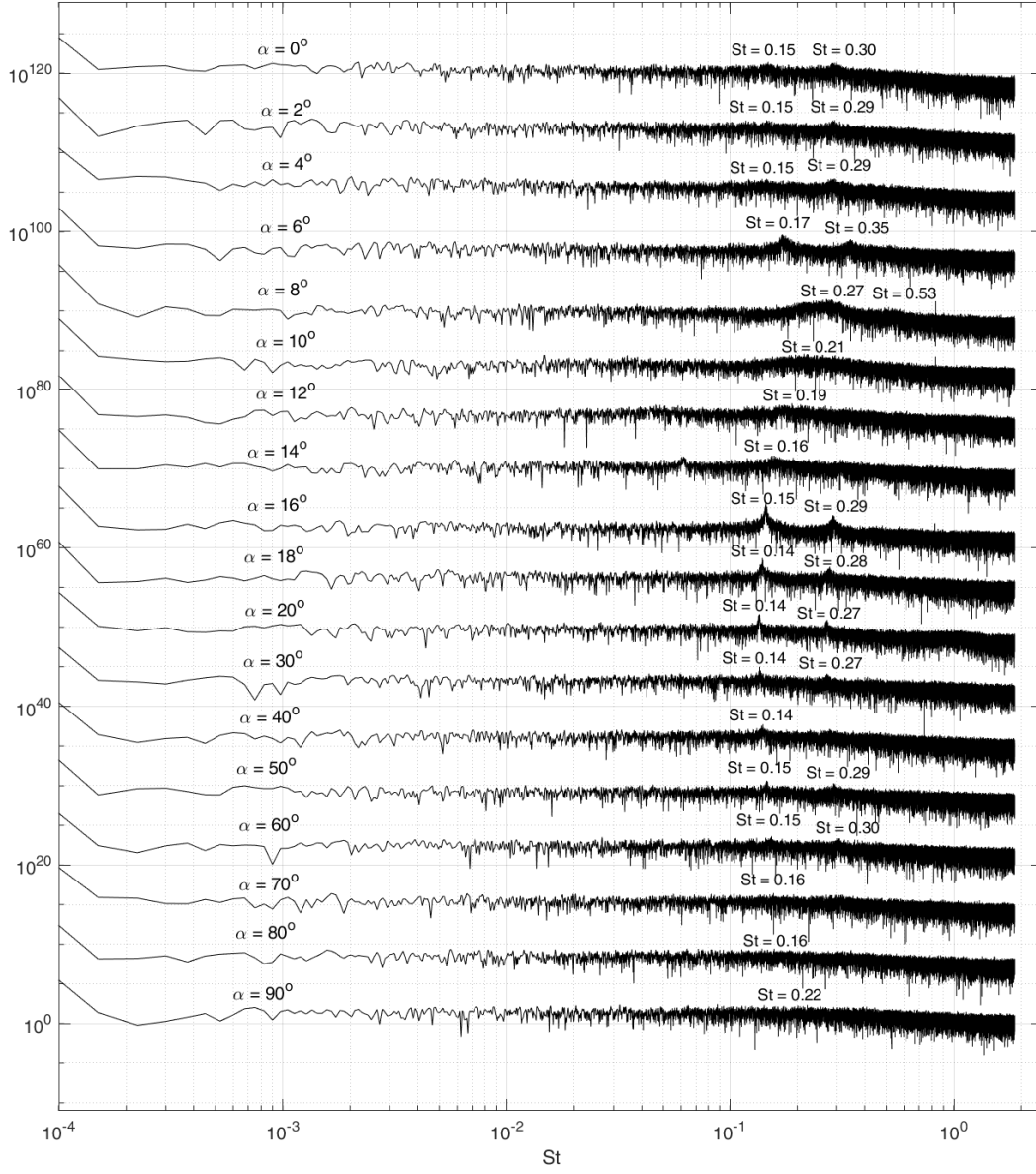


Figure C.4: St vs. α for $P/D = 2$: $Re_D = 3.98e+04$. Each power spectrum is the result of 5 averages.

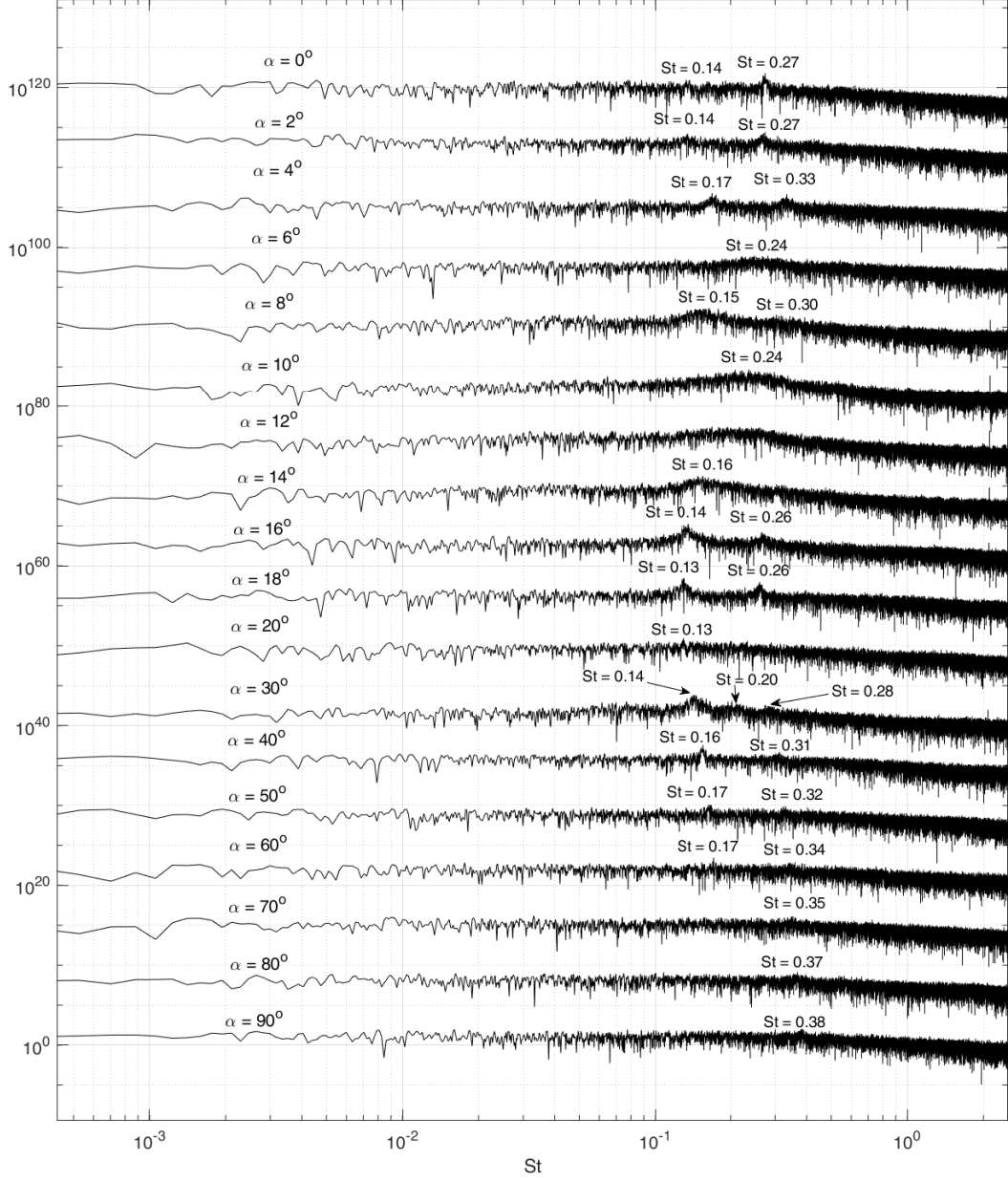


Figure C.5: St vs. α for $P/D = 3$; $Re_D = 1.70e+04$. Each power spectrum is the result of 5 averages.

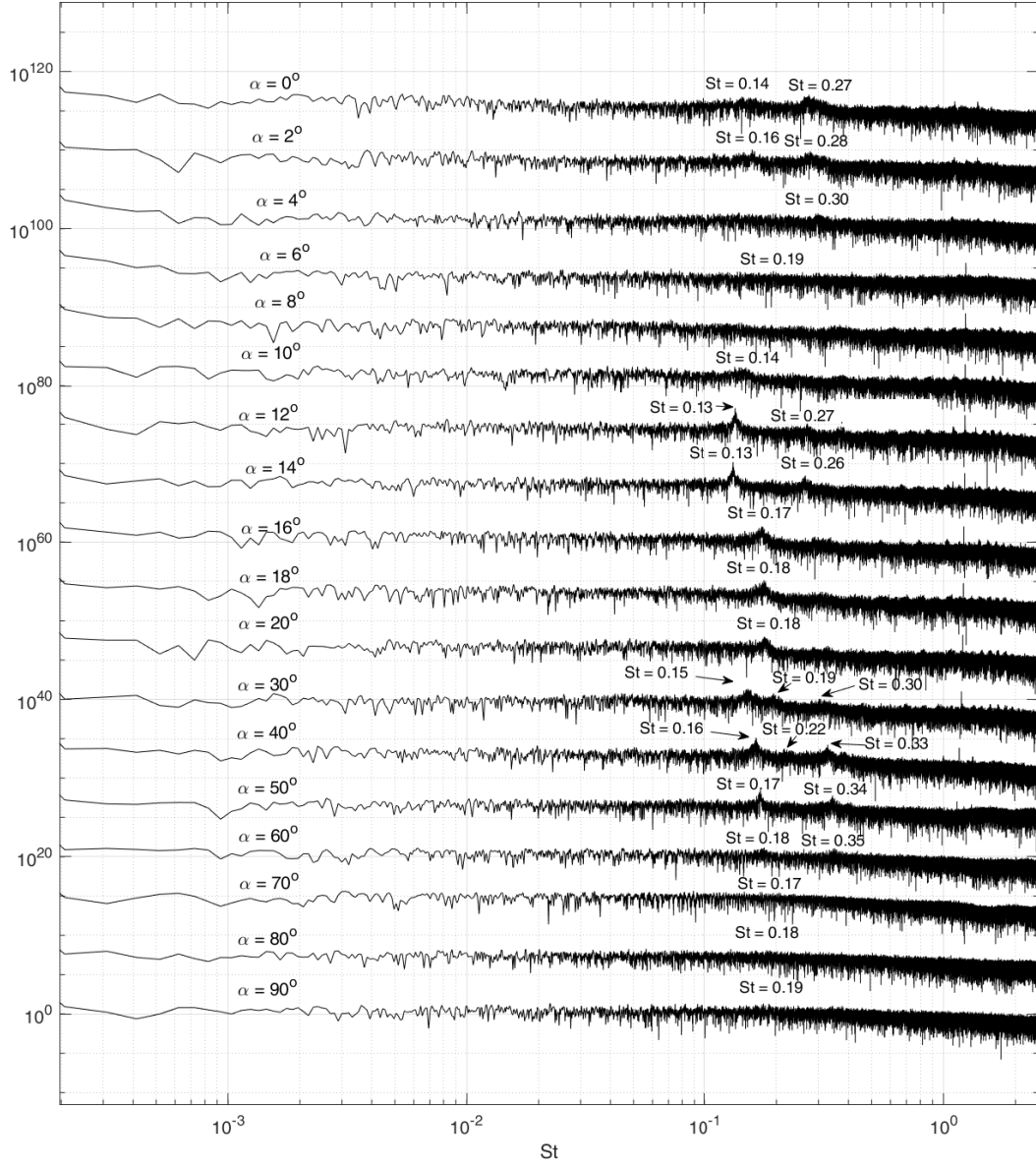


Figure C.6: St vs. α for $P/D = 3$: $Re_D = 2.89e+04$. Each power spectrum is the result of 5 averages.

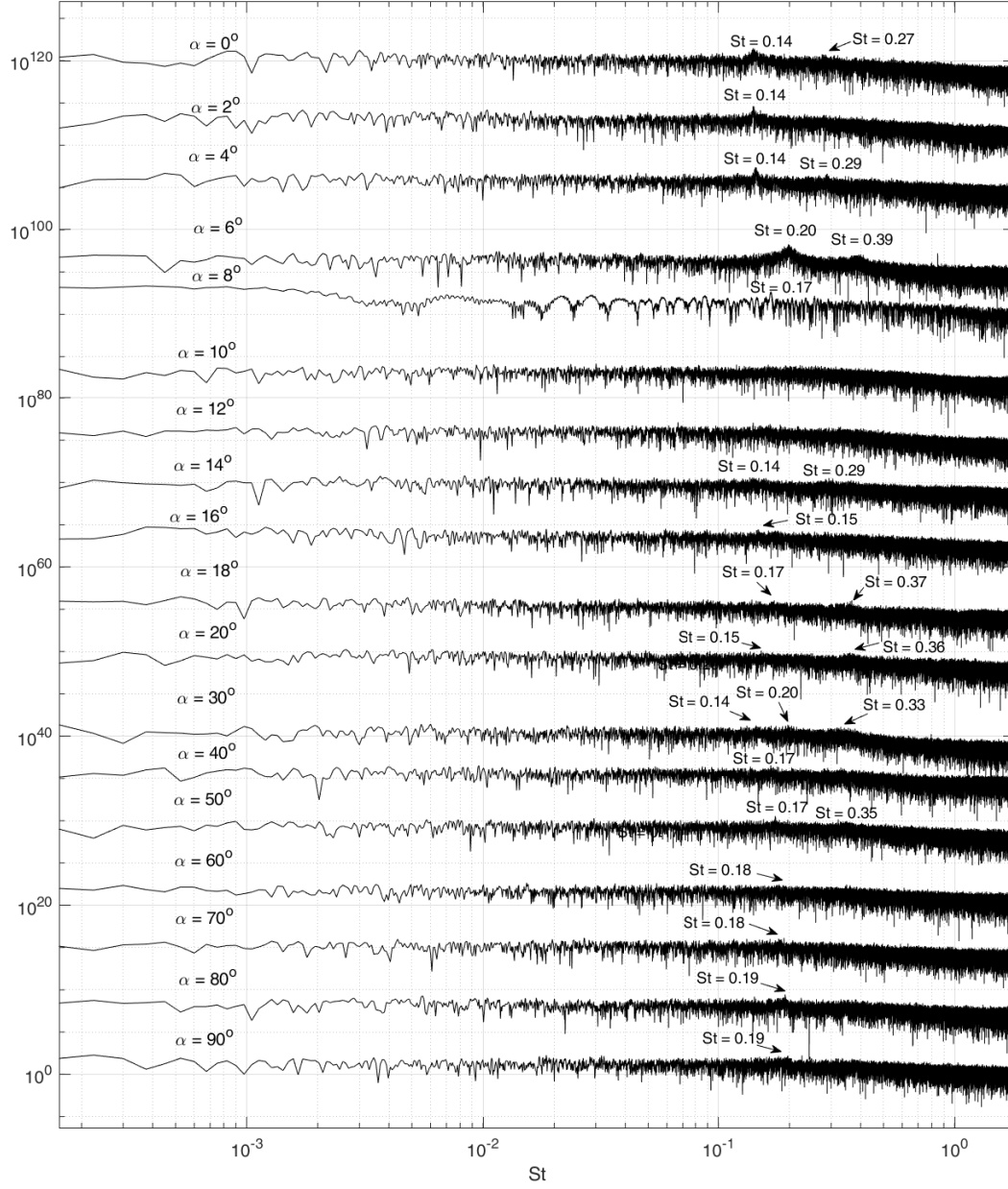


Figure C.7: St vs. α for $P/D = 3$: $Re_D = 3.98e+04$. Each power spectrum is the result of 5 averages.

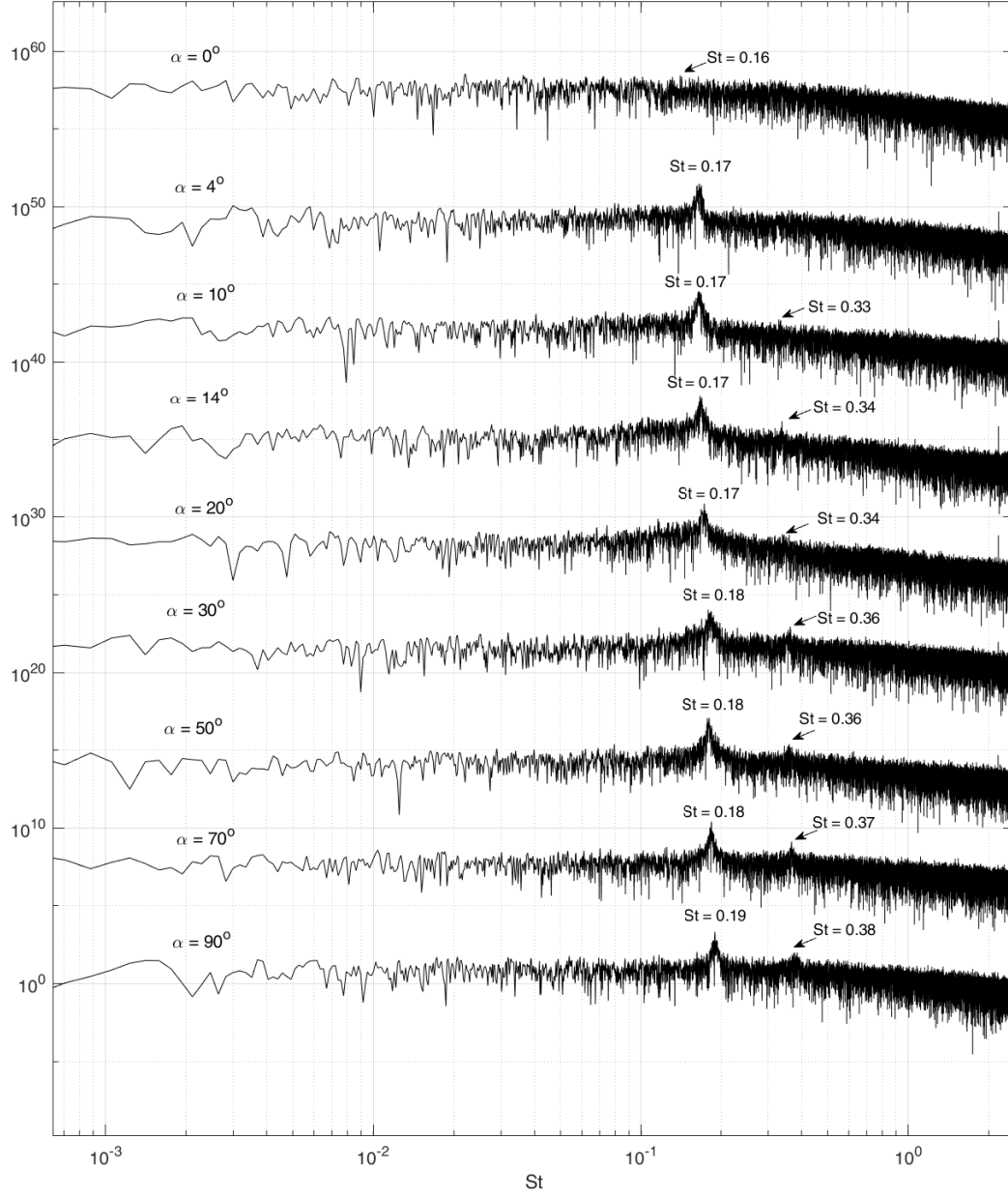


Figure C.8: St vs. α for $P/D = 4$; $Re_D = 1.70 \times 10^4$. Each power spectrum is the result of 5 averages.

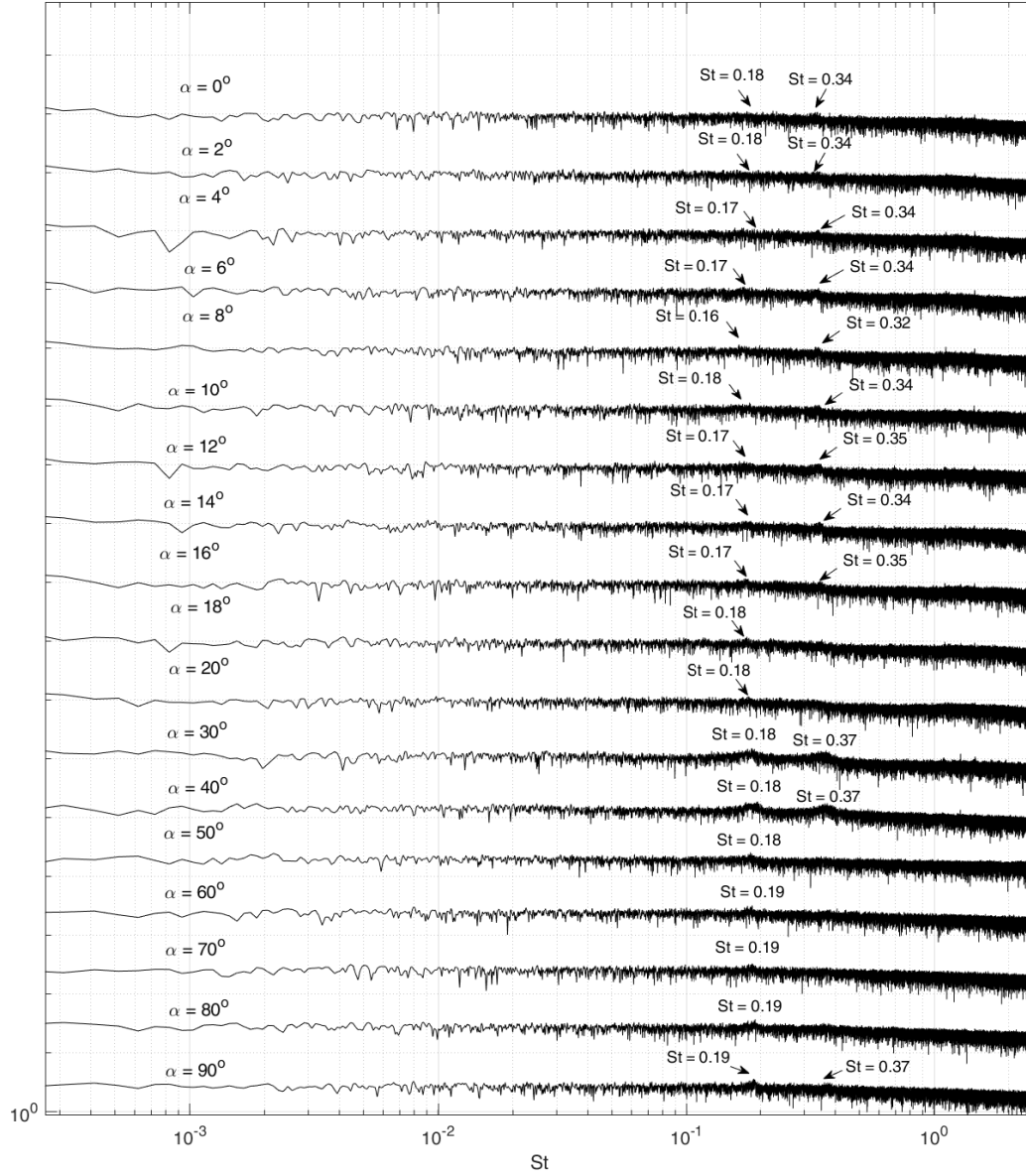


Figure C.9: St vs. α for $P/D = 4$; $Re_D = 2.89 \times 10^4$. Each power spectrum is the result of 5 averages.

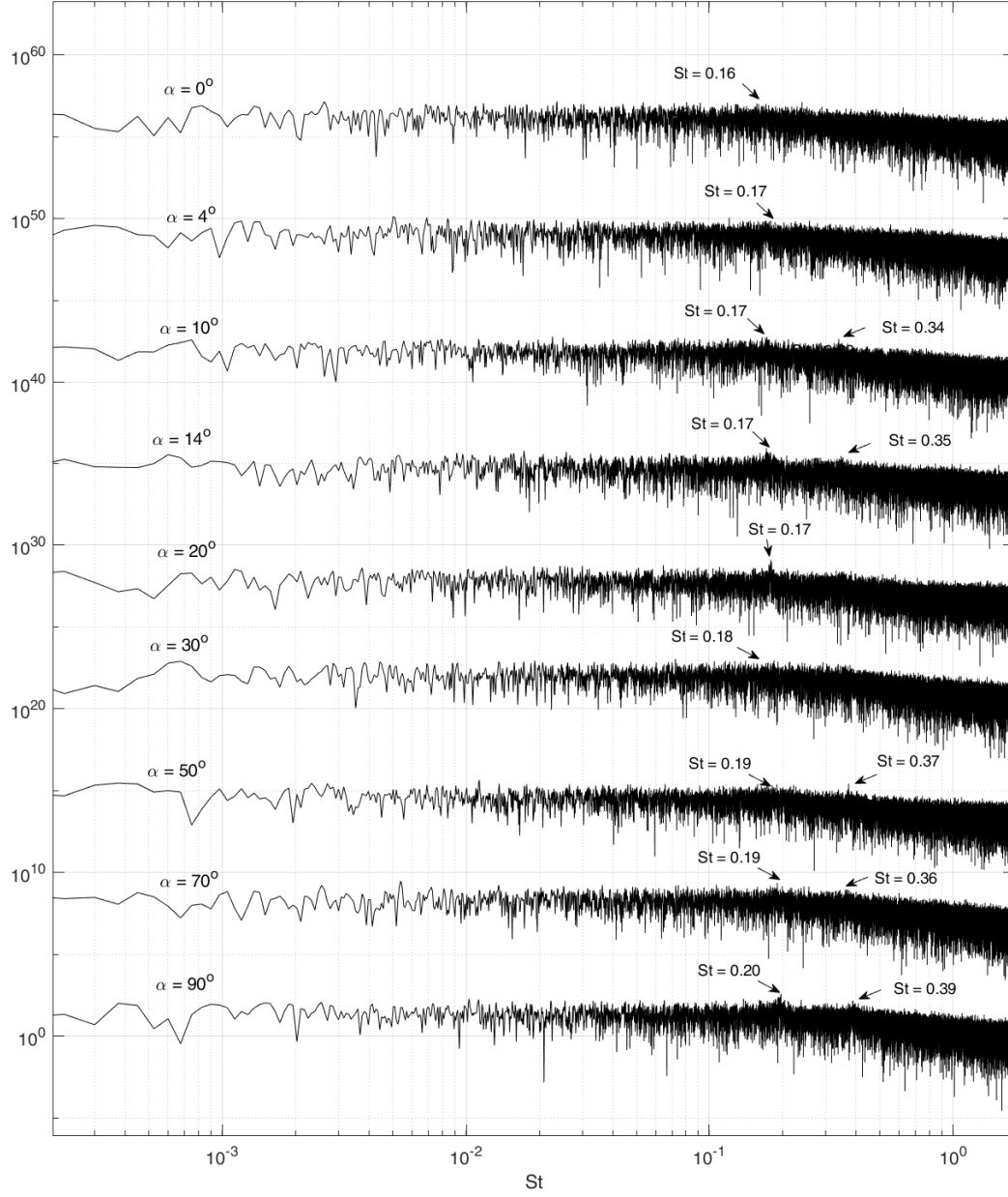


Figure C.10: St vs. α for $P/D = 4$; $Re_D = 3.98e+04$. Each power spectrum is the result of 5 averages.

D MATLAB Code

D.1 Create power spectra and locate peaks

```
1  clc
2  clear
3
4
5  clf
6
7  tic
8
9
10 filename_1 = '\\samba1\cclark\dcengr\Desktop\Graduate ...
    Research\PD3\5_9\PD3_59_hw_fs5k_N50k_25hz.xlsx';
11
12 %xlRange = 'A2:Z500001';
13 xlRange = 'A2:R50001';
14 %xlRange = 'A50001:R100001';
15 V1 = xlsread(filename_1,1,xlRange);    % import hot wire voltage readings
16
17 % Vmean = zeros(1,25);
18 % V = zeros(50000,25);
19 % u = zeros(50000,25);
20 Vmean = zeros(1,18);
21 V = zeros(50000,18);
22 u = zeros(50000,18);
23
24 %for col = 1:9
25 for col = 1:18
26 % for col = 1:26
27
28 Vmean(:,col) = mean(V1(:,col));    % calculate mean for each column
29
30 V = V1 - Vmean(:,col);            % subtract mean from voltage data
31
32
33 end
34
```

```

35 u = ((V.^2 - 3.272)./1.9926).^(1/0.5);    %convert voltage to velocity w/ ...
      King's Law
36
37
38 range1 = 1:50000;
39 range2 = 50001:100000;
40 range3 = 100001:150000;
41 range4 = 150001:200000;
42 range5 = 200001:250000;
43 range6 = 250001:300000;
44 range7 = 300001:350000;
45 range8 = 350001:400000;
46 range9 = 400001:450000;
47 range10 = 450001:500000;
48
49 range = [range1', range2', range3', range4', range5', range6', range7', ...
      range8', range9', range10'];
50
51 pxx = zeros(25001,18);
52 f = zeros(25001,18);
53 St = zeros(25001,18);
54 pks = zeros(25001,18);
55 locs = zeros(25001,18);
56
57
58 for i = 1:18
59
60
61
62
63     rng default
64     Fs = 5000;
65     N = 50000;
66     Nx = 50000;    %length(u(range10,i));
67     % Window data
68     w = hanning(Nx);
69     nfft = Nx;
70     [pxx(:,i),f(:,i)] = pwelch(u(range1,i),w,0,nfft,Fs);
71
72 %     for k = 1:5

```

```

73 %     psdav(:,k) = sum(psdu(:,k))/5;
74 %     end
75
76
77     %vel = 28.401; % Wind tunnel motor @ 35 Hz: mean wind tunnel velocity [m/s]
78     vel = 20.614; % Wind tunnel motor @ 25 Hz: mean wind tunnel velocity [m/s]
79     %vel = 12.101; % Wind tunnel motor @ 15 Hz: mean wind tunnel velocity [m/s]
80     D = 0.0213; % cylinder diameter [m]
81     St(:,i) = (f(:,i)*D)/vel; % strouhal number
82     loglog(St,pxx(:,i)*(10^(7*i)),'k')
83     xlim([10^-4 2.5])
84     %ylim([10^-5 10^180])
85     grid on
86     title([' P/D = 2: 25 Hz '])
87     xlabel('St')
88
89     hold on
90
91
92
93
94 [sortedpxx(:,i), sortedInds(:,i)] = sort(pxx(:,i),'descend');
95 top100(:,i) = sortedInds(1:100,i);
96
97 %[pks(:,i), locs(:,i)] = findpeaks(pxx(:,i));
98 Stmax(:,i) = St(top100(:,i),i); %find strouhal number of maximum frequency ...
    present in signal
99
100 end
101
102 Stmax
103
104 toc

```

D.2 Create time-synchronous averages

```

1
2 clc

```

```

3 clear
4
5 tic
6
7
8 filename_1 = '\\samba1\cclark\dcengr\Desktop\Graduate ...
           Research\PD2\5_15\PD2_515_hw_fs5k_N50k_25hz.xlsx';
9
10 xlRange = 'A2:R500001';
11
12 V1 = xlsread(filename_1,1,xlRange); % import hot wire voltage readings
13
14 Vmean = zeros(1,25);
15 V = zeros(500000,25);
16 u = zeros(500000,25);
17
18 % for col = 1:18
19 %
20 % Vmean(:,col) = mean(V1(:,col)); % calculate mean for each column
21 %
22 % V = V1 - Vmean(:,col); % subtract mean from voltage data
23 %
24 % end
25
26 V = V1;
27
28 u = ((V.^2 - 3.272)./1.9926).^(1/0.5); %convert voltage to velocity w/ ...
           King's Law
29
30
31 Fs = 5000;
32 t = 0:1/Fs:10-1/Fs; % signal sampled at 5000 Hz for 10 s
33
34 F01 = 187.99; % frequency associated with St = 0.194256 for P/D = 2 @ 90 degrees
35
36 subplot(2,1,1)
37
38 plot(t,u(1:50000,1))
39 xlim([0 1/F01])
40 ylim([19 22])

```

```

41 tPulse1 = 0:1/F01:max(t);
42
43 ylabel('Amplitude [m/s]')
44 title('Angle = 90 degrees')
45
46 tsa(u(1:50000,1),Fs,tPulse1, 'Method', 'fft')
47
48
49
50 hold on
51
52
53 F02 = 128.6;
54
55 subplot(2,1,2)
56
57 plot(t,u(1:50000,7))
58 xlim([0 1/F02])
59 ylim([19 22])
60 tPulse2 = 0:1/F02:max(t);
61
62 ylabel('Amplitude [m/s]')
63 title('Angle = 30 degrees')
64 tsa(u(1:50000,7),Fs,tPulse2, 'Method', 'fft')
65
66
67 toc

```